



# Wireless multilateral devices for optogenetic studies of individual and social behaviors

Yiyuan Yang <sup>1,27</sup>, Mingzheng Wu <sup>2,27</sup>, Abraham Vázquez-Guardado <sup>3,27</sup>, Amy J. Wegener <sup>4,5</sup>, Jose G. Grajales-Reyes <sup>6</sup>, Yujun Deng<sup>1,7,8,9</sup>, Taoyi Wang<sup>10</sup>, Raudel Avila<sup>1,3,8,9</sup>, Justin A. Moreno<sup>4,5,11</sup>, Samuel Minkowicz <sup>2</sup>, Vasin Dumrongprechachan<sup>2,12</sup>, Jungyup Lee<sup>13</sup>, Shuangyang Zhang<sup>1,3,8,9,14</sup>, Alex A. Legaria<sup>6</sup>, Yuhang Ma<sup>15</sup>, Sunita Mehta<sup>16</sup>, Daniel Franklin<sup>3,9</sup>, Layne Hartman<sup>17</sup>, Wubin Bai <sup>3,9</sup>, Mengdi Han<sup>3</sup>, Hangbo Zhao <sup>3</sup>, Wei Lu<sup>3</sup>, Yongjoon Yu<sup>12</sup>, Xing Sheng <sup>18</sup>, Anthony Banks<sup>3,13,19</sup>, Xinge Yu <sup>20</sup>, Zoe R. Donaldson <sup>21</sup>, Robert W. Gereau IV <sup>6</sup>, Cameron H. Good<sup>3,4,5</sup>, Zhaoqian Xie <sup>22</sup>✉, Yonggang Huang <sup>1,3,8,9</sup>✉, Yevgenia Kozorovitskiy <sup>2,12</sup>✉ and John A. Rogers <sup>1,9,13,17,19,23,24,25,26</sup>✉

Advanced technologies for controlled delivery of light to targeted locations in biological tissues are essential to neuroscience research that applies optogenetics in animal models. Fully implantable, miniaturized devices with wireless control and power-harvesting strategies offer an appealing set of attributes in this context, particularly for studies that are incompatible with conventional fiber-optic approaches or battery-powered head stages. Limited programmable control and narrow options in illumination profiles constrain the use of existing devices. The results reported here overcome these drawbacks via two platforms, both with real-time user programmability over multiple independent light sources, in head-mounted and back-mounted designs. Engineering studies of the optoelectronic and thermal properties of these systems define their capabilities and key design considerations. Neuroscience applications demonstrate that induction of interbrain neuronal synchrony in the medial prefrontal cortex shapes social interaction within groups of mice, highlighting the power of real-time subject-specific programmability of the wireless optogenetic platforms introduced here.

Understanding the functional organization of the central nervous system is a major goal in modern neuroscience research<sup>1</sup>. In vivo optogenetics facilitates this goal by modulating neuronal activity using light stimulation of genetically targeted excitatory or inhibitory opsins<sup>2–4</sup>. However, the most common approach, using optical fibers to deliver light from external sources<sup>5,6</sup>, results in steric constraints that can interfere with animals' natural movements and impede the investigation of neural circuits underlying complex behaviors<sup>7–9</sup>. Recently developed, battery-free wireless devices that incorporate microscale light-emitting diodes ( $\mu$ -ILEDs) and radiofrequency (RF) strategies for wireless power delivery enable fully implantable, tether-free

optogenetic studies<sup>7,8,10,11</sup>. The most advanced system variants provide control over optical intensity, pulse duration and stimulation frequency, with some level of multimodal operation<sup>10</sup>; yet, they rely on passive modulation of the RF source or deterministic preloaded programs in microcontrollers. These control mechanisms limit real-time modification of stimulation protocols during the course of an experiment. Moreover, the geometrical designs of current wireless platforms allow for only single- or dual-probe placement with fixed spacing<sup>8–10</sup>, restricting flexible targeting in the brain and periphery. Finally, while subdermal mounting on the head of the animal is straightforward, the location imposes severe constraints on the area available for circuit components and receiver antennas.

<sup>1</sup>Department of Mechanical Engineering, Northwestern University, Evanston, IL, USA. <sup>2</sup>Department of Neurobiology, Northwestern University, Evanston, IL, USA. <sup>3</sup>Center for Bio-Integrated Electronics, Northwestern University, Evanston, IL, USA. <sup>4</sup>US Army Research Laboratory, Aberdeen Proving Ground, MD, USA. <sup>5</sup>US Army Medical Research Institute of Chemical Defense, Aberdeen Proving Ground, MD, USA. <sup>6</sup>Washington University Pain Center and Department of Anesthesiology, Washington University, St. Louis, MO, USA. <sup>7</sup>State Key Laboratory of Mechanical System and Vibration, Shanghai Jiao Tong University, Shanghai, China. <sup>8</sup>Department of Civil and Environmental Engineering, Northwestern University, Evanston, IL, USA. <sup>9</sup>Department of Materials Science and Engineering, Northwestern University, Evanston, IL, USA. <sup>10</sup>Department of Physics, Tsinghua University, Beijing, China. <sup>11</sup>SURVICE Engineering, Belcamp, MD, USA. <sup>12</sup>Chemistry of Life Processes Institutes, Northwestern University, Evanston, IL, USA. <sup>13</sup>Neurolux Inc, Evanston, IL, USA. <sup>14</sup>School of Civil Engineering, Southwest JiaTong University, Chengdu, China. <sup>15</sup>School of Chemical Engineering and Technology, Tianjin University, Tianjin, People's Republic of China. <sup>16</sup>CSIR-Central Scientific Instruments Organization, Ministry of Science & Technology, Sector 30-C, Chandigarh, India. <sup>17</sup>Department of Biomedical Engineering, Northwestern University, Evanston, IL, USA. <sup>18</sup>Department of Electronic Engineering, Tsinghua University, Beijing, China. <sup>19</sup>Simpson Querrey Institute & Feinberg Medical School, Northwestern University, Evanston, IL, USA. <sup>20</sup>Department of Biomedical Engineering, City University of Hong Kong, Kowloon Tong, Hong Kong. <sup>21</sup>Psychology and Neuroscience, Molecular Cellular and Developmental Biology, University of Colorado Boulder, Boulder, CO, USA. <sup>22</sup>State Key Laboratory of Structural Analysis for Industrial Equipment, Department of Engineering Mechanics, Dalian University of Technology, Dalian, P.R. China. <sup>23</sup>Department of Chemistry, Northwestern University, Evanston, IL, USA. <sup>24</sup>Department of Neurological Surgery, Northwestern University, Evanston, IL, USA. <sup>25</sup>Department of Electrical and Computer Engineering, Northwestern University, Evanston, IL, USA. <sup>26</sup>Department of Computer Science, Northwestern University, Evanston, IL, USA. <sup>27</sup>These authors contributed equally: Yiyuan Yang, Mingzheng Wu, Abraham Vázquez-Guardado. ✉e-mail: [zxie@dlut.edu.cn](mailto:zxie@dlut.edu.cn); [y-huang@northwestern.edu](mailto:y-huang@northwestern.edu); [yevgenia.kozorovitskiy@northwestern.edu](mailto:yevgenia.kozorovitskiy@northwestern.edu); [jrogers@northwestern.edu](mailto:jrogers@northwestern.edu)

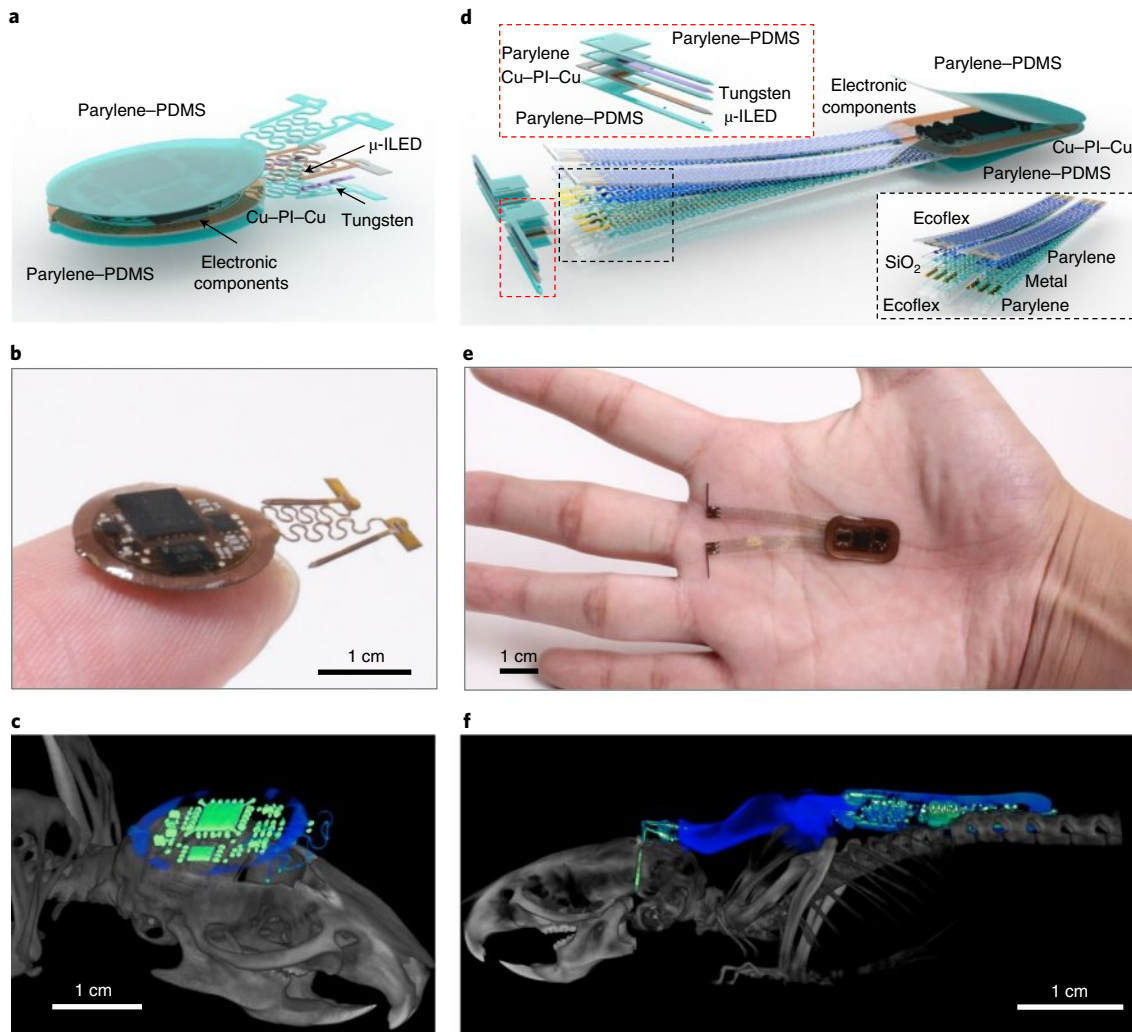


**Fig. 1 | Device layout and implantation.** **a**, Layered schematic illustration of an HM, subdermal device for optogenetic research in untethered animals with dynamically programmable operation. PI, polyimide. **b**, Photograph of the HM device. **c**, CT image of an HM device (**b**) in a mouse model. **d**, Layered schematic illustration of a similar device with a BM, subdermal design. **e**, Photograph of the BM device. **f**, CT image of a BM device (**e**) in a mouse model.

These collective limitations are important for many experimental protocols, including those that require control capabilities for independent modulation of neuronal activity patterns across regions<sup>12–15</sup> and/or real-time programmability of light delivery to interrogate causal relationships between neuronal activity and behavioral phenotypes<sup>16–19</sup>. Also, independent wireless control over multiple individual animals within the same physical space could create unique opportunities to investigate social behavior<sup>20,21</sup>. The overall capabilities of the technology introduced here address these requirements, with potential for low-cost production using advanced manufacturing processes, adapted from the flexible printed circuit board industry, suggesting a strong potential for widespread adoption across the neuroscience community.

## Results

**Head-mounted and back-mounted multilateral optogenetic devices.** The devices described here include both head-mounted (HM) and back-mounted (BM) designs (Fig. 1 and Extended Data Fig. 1a). The devices are wirelessly powered using magnetic inductive coupling provided by a primary dual-loop RF transmission antenna driven at 13.56 MHz and wrapped around the experimental enclosure ( $\sim 30 \times 30 \text{ cm}^2$ ). The user interface controls the near-field communication (NFC) protocol that allows

independent wireless communication to each device through the same transmission antenna in real time. Figure 1a shows an expanded schematic illustration of the HM device ( $10 \times 12 \text{ mm}^2$ ,  $\sim 1.2 \text{ mm}$  thick). The small size allows implantation directly over the top of the skull, underneath the skin, in animal models as small as mice. The device contains a laser-ablated receiver antenna with soldered electronic components to provide power and active control. μ-ILEDs affixed at the tip ends of the penetrating probes provide localized illumination for stimulation or inhibition. Bilateral probes connected to the electronic platform via independent serpentine traces provide large degrees of freedom in positioning during surgical processes. A parylene ( $\sim 14 \mu\text{m}$ )-polydimethylsiloxane (PDMS;  $\sim 30 \mu\text{m}$  at probes and serpentine traces and  $\sim 200$ – $800 \mu\text{m}$  elsewhere) bilayer encapsulates the device and provides soft contact with surrounding tissues. The advanced HM-device platform (Fig. 1b) incorporates an analog filter, an NFC system-on-a-chip and a microcontroller for dynamically programmable operation (Extended Data Fig. 1b) of two independent channels. Simplified versions of these devices (Supplementary Fig. 1) selectively support voltage regulation (Extended Data Fig. 1c) for experiments that only require synchronized bilateral stimulation at fixed intensity. Details of the implantation procedures are in Supplementary Figs. 2 and 3.

The lateral dimensions of HM devices cannot exceed the top surface of the skull of the animal ( $\sim 100 \text{ mm}^2$  for mice), restricting advanced embodiments with larger sizes and power requirements. A solution that largely circumvents these considerations uses the broad space on the back of the animal. Here, BM subdermal implants can include relatively large receiver coils ( $11 \times 19 \text{ mm}^2$ ) and complex electronics encapsulated in a parylene–PDMS bilayer, similar to that used in the HM devices. The penetrating probes connect to the electronic platform through thin ( $\sim 390 \text{ nm}$ ) serpentine metallic traces encapsulated in soft elastomers ( $\sim 200 \mu\text{m}$ ) to yield mechanics compatible with the implantation procedures and natural motions of the animal, without adverse effects (Fig. 1d). An example device illustrating this design offers dynamically programmable operation (Extended Data Fig. 1b) with four independent  $\mu$ -ILEDs (Fig. 1e). The layouts can be further extended to  $\mu$ -ILED arrays that integrate injectable probes or compliant substrates at additional interface locations, including peripheral nerves, heart, spinal cord and others. Detailed surgical procedures for mice and rats appear in Supplementary Figs. 4 and 5. Microscale computed tomography (CT) images of mice with the HM or BM implants are shown in Fig. 1c,f. Studies indicate chronic stability in operation for  $>9$  weeks, the longest tested period. Additional information on device fabrication is in Supplementary Figs. 6–8 and the Methods section.

**Mechanical characterization for multilateral optogenetic devices.** Electrical connections between the electronics and the probes for BM devices must support a wide range of continuous motion across the back and neck regions during natural movement. Videographic analyses using DeepLabCut<sup>22</sup> yielded quantitative estimates of the range of deformations associated with natural mouse motion at the head, neck, back and tail regions (Fig. 2a and Methods), thereby defining compliance requirements in the interconnect structures. Specifically, changes in distances from head to neck and from neck to back determine the magnitudes of compression and elongation. Variations in the circumradius of the head–neck–back triangle determine the levels of bending. The probability distribution in Fig. 2b shows ranges of  $\sim 30\%$  for compression and  $\sim 60\%$  for elongation. Figure 2c highlights the corresponding probability distribution for bending, ranging from  $\sim 1 \text{ cm}$  to  $\sim 30 \text{ cm}$ .

The designs of the interconnects of the BM devices support repetitive deformations across these ranges. Finite element analysis (FEA) and experimental results showed that the constituent materials of the interconnects remain in an elastic response regime for uniaxial stretching of up to 50% and for  $95^\circ$  bending at a radius of curvature of 2.5 mm (Fig. 2d,e). The equivalent strains in the metals remain less than their yield strains ( $\sim 0.3\%$ )<sup>23</sup>, as were the strains in the polymers. Systematic experimental studies using cyclic tests (10,000 cycles, 1 Hz) at different stretching levels defined the transition threshold from elastic to plastic deformation. In the elastic

region, the electrical resistance of the interconnects remained nearly unchanged. Plastic deformations lead to notable increases in resistance. The results, highlighted in Fig. 2b (black line), define an elastic range that extended to a stretch of  $\sim 50\%$  (resistance change  $<3\%$ ), consistent with FEA results (Fig. 2d). Unlike for BM devices, the serpentine traces in the HM devices can be plastically deformed to target positions during implantation because they remain fixed in these positions by anchoring to the skull with dental cement (Supplementary Figs. 2 and 3). Extended Data Fig. 2 shows typical mechanical deformations for the HM devices during and after implantation, all of which lead to material strains that remain well below their fracture points<sup>24</sup>.

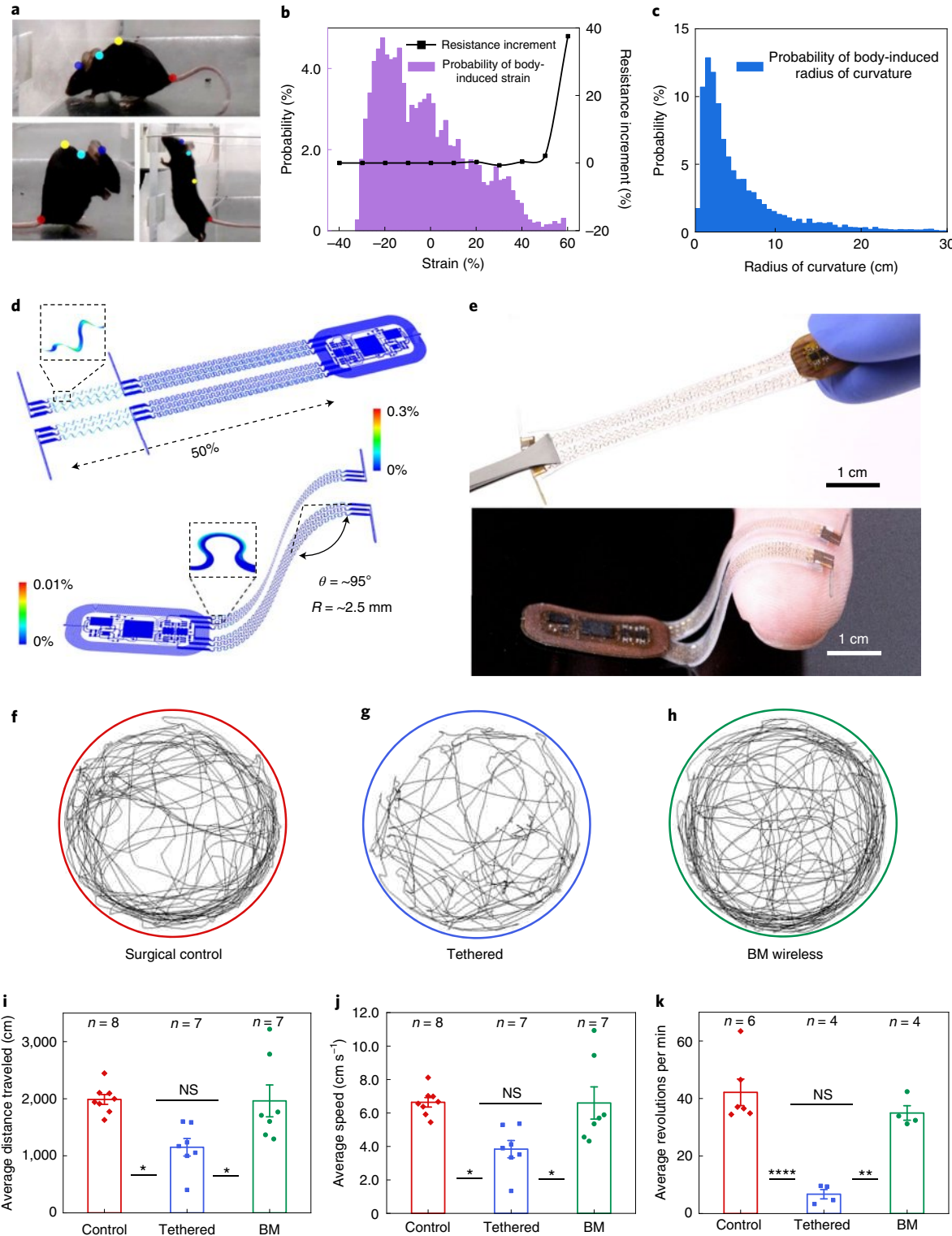
For both classes of devices, the impact on locomotor behaviors was negligible. Natural behavior patterns of mice implanted with HM devices were similar to those of mice without implantation (Extended Data Fig. 3), consistent with previous studies<sup>25</sup>. Figure 2f–h presents representative single-mouse movement tracks over a 5-min period in an open-field environment. Reductions in the average distance traveled (Fig. 2i; ANOVA,  $F=6.607$ ,  $P=0.0066$ ) and average speed during movements (Fig. 2j; ANOVA,  $F=6.418$ ,  $P=0.0074$ ) occurred for mice implanted with and tethered by optical fibers. Meanwhile, mice implanted with BM devices exhibited near-identical travel distances (not significant,  $P=0.99$ ) and movement speeds (not significant,  $P=0.99$ ) compared to surgical controls. Additional tests examined mobility across the groups ( $n=4–6$ ) using a running wheel experiment. Mice implanted with BM devices exhibited similar average revolutions per minute as controls over a 60-min period (not significant,  $P=0.40$ ), while tethered mice ran less than those in control and BM groups (Fig. 2k; ANOVA,  $F=23.12$ ,  $P=0.0001$ ). Collectively, these experiments demonstrate that BM devices do not restrict natural animal movement and maintain function during routine activity.

**Biocompatibility characterization for multilateral optogenetic devices.** Additional experiments assessed the biocompatibility of the implantable device components, including the injectable probes with tungsten stiffeners and BM subdermal implants. Immunohistochemical markers of glial cells and hemoglobin yielded insights into implantation-associated gliosis and hemorrhage. Mice implanted with wireless probes or optical fibers  $200 \mu\text{m}$  in diameter showed similar astrocytic and microglial activation (Extended Data Fig. 4a–e). No differences in hemoglobin immunoreactivity between conditions was observed (Extended Data Fig. 4f). The wireless probes did not induce significant damage to the brain tissue, as the ratio of measured damage and estimated damage was  $\sim 1$  (Extended Data Fig. 4g). These data suggest that the biocompatibility of wireless probes with encapsulated tungsten is similar to that of optical fiber.

**Fig. 2 | Characterization of mechanical properties and effects on animal locomotor behavior.** **a**, Photograph of the curvature of the body of a mouse and changes in this curvature during natural movements. The colored dots mark points on the head, neck, back and tail of the mouse for characterizing these changes as the mouse moves in an enclosure. **b**, Probability distribution of tensile strains (that is, compressing and stretching) associated with routine activities and benchtop tests of changes in resistance of the stretchable interconnects used for the BM-device platform after 10,000 cycles of stretching and compressing (black line) at 1 Hz. **c**, Corresponding probability distribution of bending deformations (that is, radius of curvature). **d**, FEA simulations of a stretched and bent BM device. **e**, Photographs of a stretched and bent device. **f–h**, Results of motion tracking (5 min in a circular arena) for independent, freely moving mice (surgical control), for mice implanted with bilateral optical fibers (tethered) and for mice implanted with BM devices (BM wireless). **i,j**, The same cohorts of biologically independent animals (control,  $n=8$ ; tethered,  $n=7$ ; BM wireless,  $n=7$ ) were used to derive these results over three independent experiments. **i**, Average distance traveled over 5 min in the circular arena (one-way ANOVA, Tukey's multiple-comparisons test; control versus tethered,  $P=0.01$ ; tethered versus BM wireless,  $P=0.02$ ; control versus BM wireless,  $P=0.99$ ). NS, not significant. **j**, Average movement speed over 5 min in the circular arena (one-way ANOVA, Tukey's multiple-comparisons test; control versus tethered,  $P=0.02$ ; tethered versus BM wireless,  $P=0.02$ ; control versus BM wireless,  $P=0.99$ ). **k**, Average revolutions per minute when running on a wheel over a 60-min period (one-way ANOVA, Tukey's multiple-comparisons test; control versus tethered,  $P<0.0001$ ; tethered versus BM wireless,  $P=0.0014$ ; control versus BM wireless,  $P=0.40$ ). Biologically independent animals (control,  $n=6$ ; tethered,  $n=4$ ; BM wireless,  $n=4$ ) were used to derive these results over three independent experiments. All data are represented as mean  $\pm$  s.e.m. \* $P<0.05$ , \*\* $P<0.01$ , \*\*\* $P<0.0001$ .

To determine whether BM implants induce erosion of proximal tissue or spinal impact, BM-device-implanted and sham surgery control mice were compared 40 d after implantation (Extended Data Fig. 4h). No significant differences in morphology of surrounding muscles and skin, evidenced by hematoxylin and eosin staining, were observed in implanted mice compared to controls (Extended Data Fig. 4i–k). MicroCT imaging results confirmed no significant changes in bone density associated with the implants (Extended Data Fig. 4l).

**Dynamically programmable multichannel operation.** The technology introduced here supports bidirectional wireless communication, qualitatively expanding device functionality beyond that possible with previously reported technologies. The result provides full and continuous real-time wireless control over all relevant optogenetic stimulation parameters, including intensity, frequency and duty cycle. Additional capabilities include nearly arbitrary implementation of multichannel operation (unilateral or



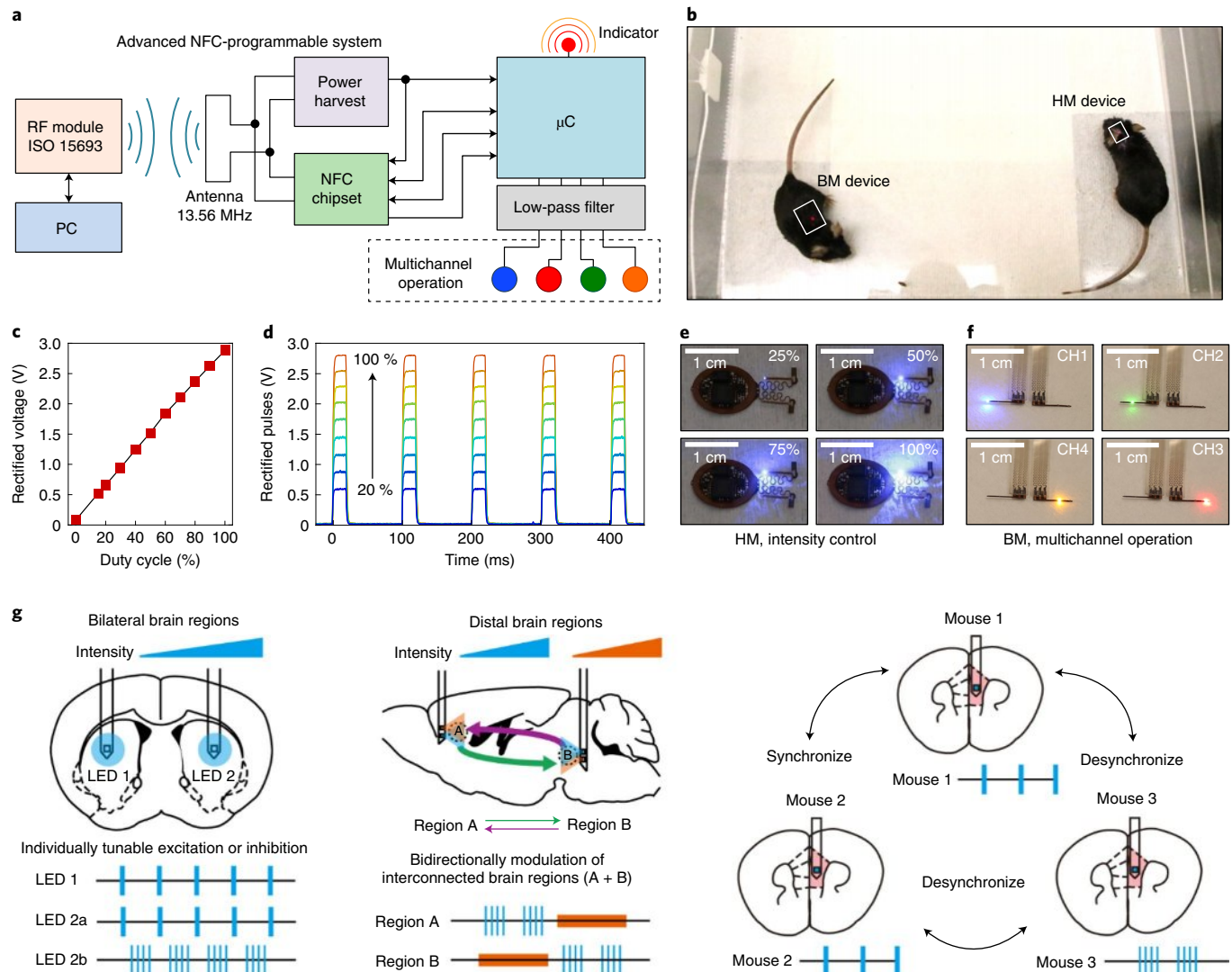


**Fig. 3 | Designs, operational features and use cases for dynamically programmable NFC electronics.** **a**, Block diagram of an NFC-enabled platform for independent, programmable control over operational parameters. Microcontroller firmware coupled with this electronic module allows multichannel selection and control over the period ( $T$ ), duty cycle and intensity of the  $\mu$ -ILEDs. PC, personal computer;  $\mu$ C, microcontroller. **b**, Photograph of HM and BM devices implemented with dynamically programmable NFC electronics, operating after implantation in mice. **c**, Filter output voltage as a function of duty cycle of the intensity-encoding carrier waveform (Extended Data Fig. 5b). **d**, Time dependence of output waveforms with a period of 100 ms and a duty cycle of 20% at various peak voltage magnitudes. The carrier frequency is 2 kHz, and the duty cycle varies from 20% to 100%. **e**, Sequence of photographs of an HM device operated at different duty cycles of the carrier waveform, to control the intensity of one of the two  $\mu$ -ILEDs. **f**, Sequence of photographs of a BM device showing multichannel operation. **g**, Schematic illustrations of several potential applications of this technology in optogenetic studies, including tunable modulation of bilateral brain regions (left), bidirectional modulation of distal regions (middle) and multi-brain synchrony manipulation (right).

bilateral stimulation) and control over multiple devices within the same enclosed space. The elements that enable these capabilities include an NFC read–write random access memory (M24LR04E, STMicroelectronics) and an eight-bit microcontroller (ATtiny84, Atmel). Extended Data Fig. 1 shows the generic electronic diagram. The user addresses the microcontroller firmware using a personal computer running a customized graphical user interface (GUI) that interfaces with the RF power and communication module, supporting the ISO 15693 NFC protocol (LRM2500-A, Feig Electronics). Upon a wireless command, the microcontroller reads operational parameters from the NFC memory (period, duty cycle, intensity and mode of operation), which are then updated into the firmware to operate up to four channels independently (Fig. 3a). Figure 3b shows mice implanted with HM and BM devices inside a cage.

Each channel in the microcontroller supports an amplitude-modulated digital signal (AM-DS) at its general purpose input/output, which controls dynamics for optical stimulation and the optical intensity of the corresponding  $\mu$ -ILED. Extended Data Fig. 5a shows schematic illustrations of time traces of the AM-DS. Here, a low-frequency signal (signal, period,  $T_1$ ; duty cycle,  $DC_1$ ) modulates a high-frequency signal (carrier, period,  $T_2$ ; duty cycle,  $DC_2$ ). The former encodes the pulse duration and frequency of the stimulation, while the latter encodes voltage control. These parameters are extracted using a second-order passive low-pass filter that performs digital-to-analog conversion in the time domain. Consider an arbitrary AM-DS, as depicted in Extended Data Fig. 5a, for which the time-dependent amplitude  $A(t)$  can be described in a Fourier series as

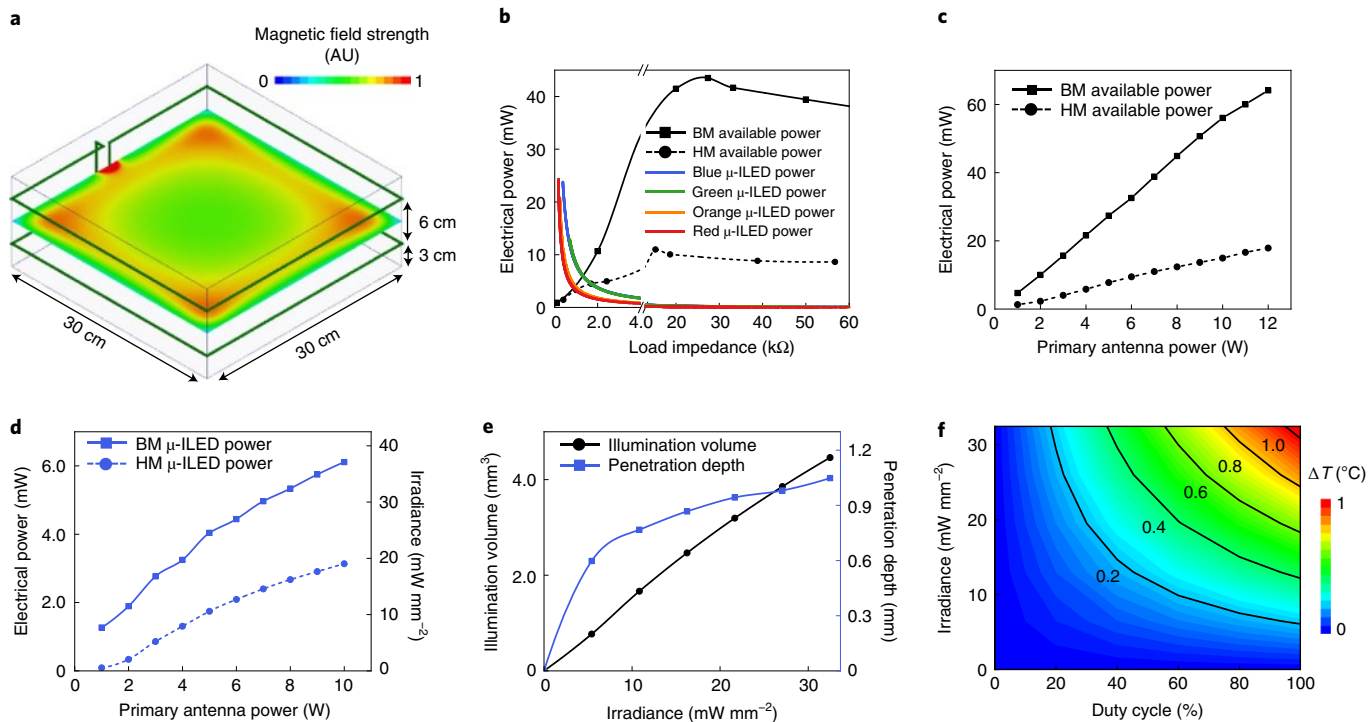


**Fig. 4 | Characterization of optical and thermal properties.** **a**, Simulated magnetic-field-intensity distribution at the central plane of a cage (dimensions, 30 cm (length) × 30 cm (width) × 15 cm (height)) surrounded by a double-loop antenna at heights of 3 cm and 9 cm. AU, arbitrary units. **b**, Electrical power supplied to HM and BM coils and different μ-ILEDs (460 nm, 535 nm, 595 nm, 630 nm) as a function of internal working impedance at 8 W of RF power applied to the transmission antenna. **c**, Maximum harvested power as a function of RF power applied to the transmission antenna for HM and BM coils. **d**, Maximum electrical and optical power for a single blue μ-ILED (460 nm) as a function of RF power applied to the transmission antenna for HM and BM devices. **e**, Illumination volume and penetration depth as a function of the output irradiance of the blue μ-ILED (460 nm) (cutoff intensity, 0.1 mW mm<sup>-2</sup>). **f**, Temperature change ( $\Delta T$  °C) at the interface between the μ-ILED and brain tissue as a function of operational irradiance of the blue μ-ILED (460 nm) and its duty cycle at a frequency of 20 Hz.

$$A(t) = A_0 \sum_{n_1=-\infty}^{\infty} C_{n_1} e^{-i\omega_{n_1} t} \sum_{n_2=-\infty}^{\infty} C_{n_2} e^{-i\omega_{n_2} t}$$

where  $A_0$  is the amplitude,  $i$  is the imaginary unit,  $n_{1,2}$ ,  $C_{n_{1,2}}$  and  $\omega_{n_{1,2}}$  ( $\omega_{n_{1,2}}=2\pi n_1 f_{n_1}, 2\pi n_2 f_{n_2}$ ) are the indices, coefficients and frequency harmonics of the signal (1) and carrier (2), respectively. The fundamental frequencies are  $f_{01}=1/T_1$  and  $f_{02}=1/T_2$ . A low-pass filter with cutoff frequency  $f_c$  larger than the signal ( $f_c > f_{01}$ ) but smaller than the carrier ( $f_c < f_{02}$ ) filters out the fundamental and higher harmonics of the carrier, while its direct current (dc) component and the low order harmonics of the signal remain, as graphically illustrated in Extended Data Fig. 5b. For a square wave, the dc component is equal to the duty cycle,  $C_{02}=DC_2$ . Thus, the AM-DS becomes a filtered low-frequency signal (with number of harmonics  $n_f$  smaller than  $f_c$ ), the amplitude of which is determined by  $DC_2$ .

$$A(t) \approx A_0 C_{02} \sum_{n_1=-n_f}^{n_f} C_{n_1} e^{-i\omega_{n_1} t}$$

The microcontroller firmware, running at 1 MHz, supports signals with periods between 1 and 65,000 ms and duty cycles between 1% and 100% and carriers with periods between 0.5 and 65 ms and duty cycles between 15% and 100%. The cutoff frequency of the second-order passive filter is designed to 700 Hz, and the carrier frequency implemented in the AM-DS is 2 kHz. Figure 3c shows the analog voltage waveform of a filtered AM-DS, for which the period and duty cycle of the signal were  $P_1=100$  ms (10 Hz) and  $DC_1=20\%$ ,

respectively. Figure 3d and Supplementary Fig. 9 show the corresponding voltage traces at different voltage levels and the pre- and post-filtered voltage traces, respectively. These results illustrate that individual channels can be driven at different voltage levels, as observed in the intensity of the blinking μ-ILED. Figure 3e displays images of an HM device with a blue μ-ILED operating at different optical intensities (Supplementary Video 1). Dynamic control over frequency and pulse duration is shown in Supplementary Videos 2 and 3. Figure 3f presents images of a BM device with four different μ-ILEDs individually activated wirelessly in an experimental enclosure (Supplementary Video 5).

This dynamic programmable NFC system offers accurate real-time wireless control over frequency ( $\pm 1.5\%$  accuracy) with pulse widths as short as 3 ms (Supplementary Fig. 10a). The pulse limit can be further reduced to 234 μs at the expense of removing the intensity-control capability. In this manner, the low-frequency component of the AM-DS involves a 1-ms temporal window that allows a single low-duty cycle oscillation of the high-frequency component (1 kHz) (Supplementary Fig. 10b). This mode of operation also enables programmable burst stimulation, for which the low-frequency component determines the burst cycles and the high-frequency component dictates the illumination dynamics.

The optogenetic device firmware allows selection across different μ-ILEDs with wide-ranging control over patterns of illumination. For example, in the HM device, four illumination configurations are possible with two independent μ-ILED channels: single-channel (unilateral) or dual-channel in-phase or 180° out-of-phase (bilateral) modes, as graphically depicted in Extended Data Fig. 5c and demonstrated in Supplementary Video 4. With arbitrary pulse-width

and frequency selection, the out-of-phase mode operation also supports variable delay operation, that is, controlling the bilateral stimulation time delay as described in Extended Data Fig. 5c. The increased available area for electronic components and harvesting power in the BM device enables operation of four independent  $\mu$ -ILEDs. Supplementary Videos 5 and 6 show example unilateral and bilateral out-of-phase modes of operation. Sixteen modes of operation are possible: four unilateral, six out-of-phase and six in-phase bilateral modes. Another feature of this technology is device-addressing capabilities. Each NFC chip is hardware encoded with a 64-bit unique identifier code that individually addresses a targeted device upon each command. The RF NFC reader can discover up to 256 devices simultaneously and communicate with any device with a known unique identifier. Supplementary Videos 7 and 8 show HM and BM devices simultaneously operating but individually controlled.

This technology expands possibilities for advanced stimulation protocols in optogenetics. Several examples are schematized in Fig. 3g. The simplest case (Supplementary Fig. 1) is synchronized excitation or inhibition of bilateral or distal brain regions. Additional possibilities (Fig. 1b) follow from regulation of neuronal activity by controlling the stimulation dynamics of  $\mu$ -ILED channels independently within the same subject. Individually tunable excitation and inhibition lines provide further controls over stimulation modes, frequencies and pulse durations, with real-time user control (Fig. 3g, left). With  $\mu$ -ILEDs of different wavelengths tailored to corresponding opsins, studies of the interactions of different brain regions in a behavioral context might exploit desynchronized patterns of optogenetic excitation or inhibition. Moreover, additional power and space provided by BM devices (Fig. 1e) allow for bidirectional modulation of interconnected brain regions, where independent, dynamic control over at least four  $\mu$ -ILEDs is important (Fig. 3g, middle). Finally, the capacity for real-time reprogramming

and independent control over multiple devices enables the studies of behaviors that involve multiple animals, each with individualized stimulation parameters (Fig. 3g, right). Additional options follow from full use of the general purpose input/output of the microcontroller for operation of up to eight channels. See Supplementary Fig. 11 and Methods for hardware implementation and customized software operation of the control system for behavior experiments.

**Optical and thermal characterization of  $\mu$ -ILEDs.** This section discusses the illumination intensity and excitation volume for given operational parameters, as well as the associated thermal loads on the adjacent tissue. Supplementary Fig. 12 summarizes current-to-voltage ( $I$ - $V$ ) measurements (Supplementary Fig. 12a) and electrical-to-optical power conversion characteristics (Supplementary Fig. 12b) for each  $\mu$ -ILED. The energy-conversion efficiency of the  $\mu$ -ILEDs determines the thermal power generated (Supplementary Fig. 12c). The efficiency of the blue (460 nm), green (535 nm), orange (590 nm) and red (630 nm)  $\mu$ -ILEDs are 36.1%, 6.6%, 6.4% and 26.7%, respectively. These parameters, together with the electrical power wirelessly harvested by the device, define the illumination intensities. Present studies consider RF power applied through an antenna on a standard experimental cage (dimensions, 30 cm (width)  $\times$  30 cm (length)  $\times$  12 cm (height)) in a double-loop configuration at heights of 3 and 9 cm from the base (Fig. 4a). Simulated results for the magnetic-field-intensity distribution at the plane in the middle between the double-loop antenna (Fig. 4a) reveal a spatially inhomogeneous magnetic field. Active voltage regulation implemented in the devices yielded constant power delivery to  $\mu$ -ILEDs throughout the experimental enclosure.

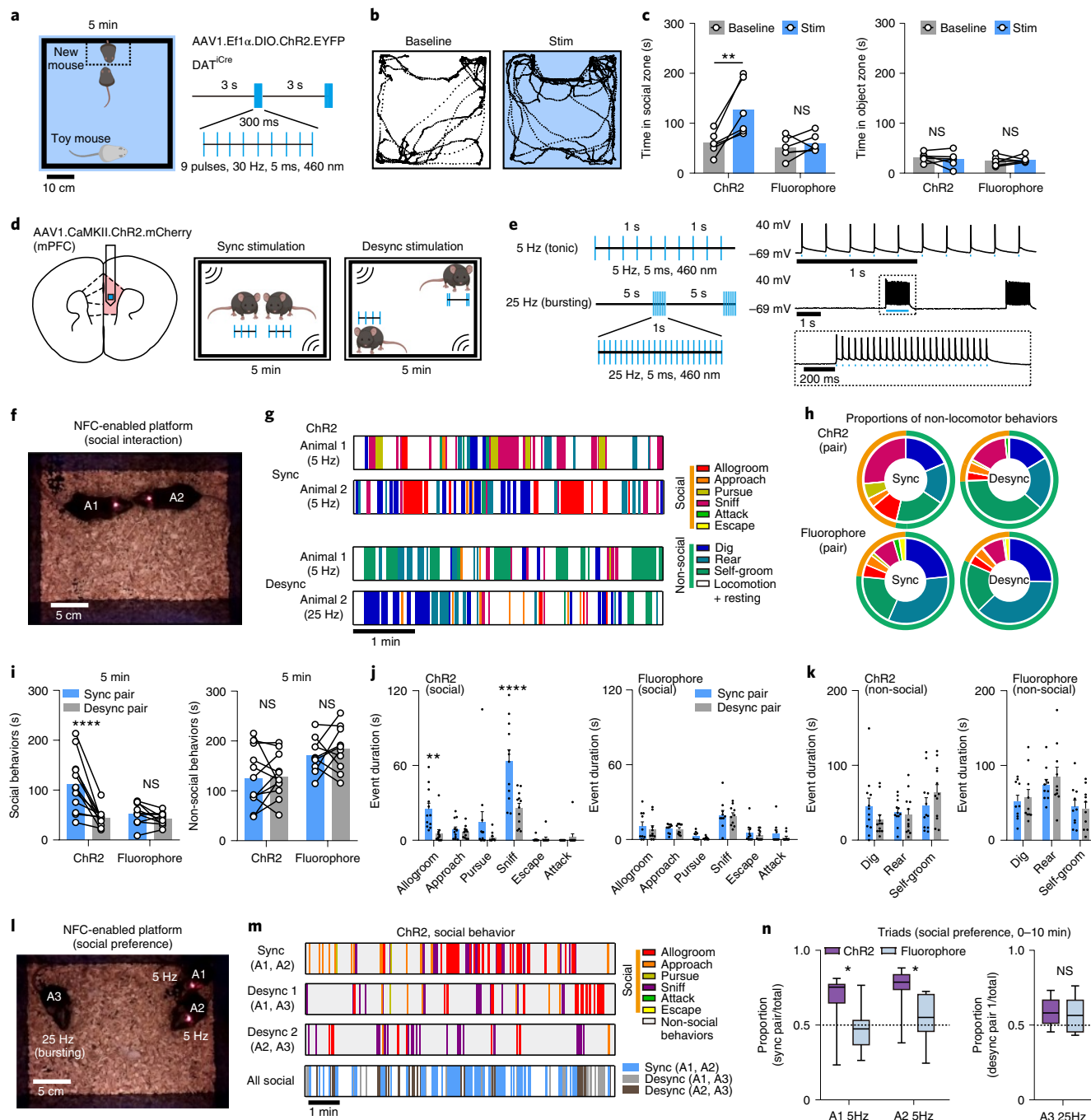
HM and BM devices have different power-harvesting capabilities due to differences in the sizes of the receiver coils. The  $I$ - $V$  characteristics of the  $\mu$ -ILEDs (Supplementary Fig. 12a) define

**Fig. 5 | Bilateral stimulation and subject-specific programmability for wireless optogenetic control of social behavior.** **a**, Left: schematic of the arena for the social preference task and the stimulation area. Right: burst pattern of wireless light stimulation (460 nm). **b**, Example traces show position tracks in baseline and bilateral stimulation conditions from one animal. **c**, Left: summary data for total time spent in the social-interaction zone in baseline and stimulation conditions. Two-way ANOVA, Sidak's multiple-comparisons test (baseline versus stim), ChR2,  $P=0.0016$ ; fluorophore,  $P=0.7763$ . Right: total time spent in the object interaction zone. Two-way ANOVA, Sidak's multiple-comparisons test (baseline versus stim), ChR2,  $P=0.6208$ ; fluorophore,  $P=0.8363$ .  $n=6$  animals per group. **d**, Left: schematic of viral transduction and probe implantation in the mPFC. Right: the arena and experimental design for the free social-interaction assay. Sync, synchronized; desync, desynchronized. **e**, Left: stimulation patterns used to induce synchronized and desynchronized activity. Right: example traces from a current-clamp recording of a ChR2-mCherry<sup>+</sup> mPFC pyramidal neuron during optogenetic activation with blue light, as noted. **f**, Photograph of two mice interacting during synchronized wireless light stimulation. **g**, Behavioral sequences recorded in individual mice receiving synchronized or desynchronized stimulation during free social interaction. **h**, Proportion of time spent engaging in non-locomotor behaviors for mice expressing ChR2 or fluorophore controls, receiving synchronized or desynchronized stimulation. Proportions of time spent engaging in social behavior: ChR2 synchronized, 46.5%; ChR2 desynchronized, 25.9%; fluorophore synchronized, 23.5%; fluorophore desynchronized, 18.4%.  $n=10\text{--}12$  pairs per group. **i**, Left: summary data show the total time spent in social interaction for paired mice during synchronized and desynchronized stimulation. Two-way ANOVA, Sidak's multiple-comparisons test (synchronized pair versus desynchronized pair), ChR2,  $P<0.0001$ ; fluorophore,  $P=0.6198$ . Right: total time spent engaging in non-social behaviors, exclusive of locomotion. Two-way ANOVA, Sidak's multiple-comparisons test (synchronized pair versus desynchronized pair), ChR2,  $P=0.9526$ ; fluorophore,  $P=0.6608$ .  $n=10\text{--}12$  pairs per group. **j**, Left: summary data for social event durations for paired ChR2-expressing mice during synchronized and desynchronized stimulation. Right: same as left but for fluorophore control mouse pairs. Two-way ANOVA, Holm-Sidak's multiple-comparisons test (synchronized pair versus desynchronized pair). ChR2: allogroom,  $P=0.0027$ ; approach,  $P=0.9517$ ; sniff,  $P<0.0001$ ; pursue,  $P=0.0939$ ; escape,  $P=0.9517$ ; attack,  $P=0.9517$ . Fluorophore: allogroom,  $P=0.8903$ ; approach,  $P=0.9541$ ; sniff,  $P=0.9541$ ; pursue,  $P=0.8996$ ; escape,  $P=0.9092$ ; attack,  $P=0.788$ .  $n=12$  pairs for ChR2 and  $n=10$  pairs for the fluorophore. **k**, Left: summary data for non-social event durations for paired ChR2-expressing mice during synchronized and desynchronized stimulation. Right: same as left but for fluorophore control mouse pairs. Two-way ANOVA, Holm-Sidak's multiple-comparisons test (synchronized pair versus desynchronized pair). ChR2: dig,  $P=0.1941$ ; rear,  $P=0.6816$ ; self-groom,  $P=0.1941$ . Fluorophore: dig,  $P=0.822$ ; rear,  $P=0.5568$ ; self-groom,  $P=0.822$ .  $n=12$  pairs for ChR2 and  $n=10$  pairs for the fluorophore. **l**, Photograph of three mice receiving 5-Hz or 25-Hz stimulation in the social-interaction arena, forming three synchronized or desynchronized pairs. **m**, Example social behavior sequences in synchronized or desynchronized pairs during free social interaction. **n**, Left: the proportion of social interactions for a focal animal in a triad with the synchronously stimulated one, over the total social-interaction time, in animals receiving 5-Hz optogenetic stimulation. Two-way ANOVA, Sidak's multiple-comparisons test, ChR2 versus fluorophore, animal (A)1,  $P=0.0145$ ; A2,  $P=0.0198$ . One-sample  $t$ -test, ChR2 versus random chance (0.5, dotted line), A1,  $P=0.0066$ ; A2,  $P=0.0003$ . Right: the proportion of social interactions for the focal animal receiving 25-Hz stimulation in a triad, desynchronized from both other present conspecifics, over the total social-interaction time. Unpaired two-tailed  $t$ -test, ChR2 versus fluorophore,  $P=0.7207$ .  $n=8\text{--}10$  experiments per group. Data represent mean  $\pm$  s.e.m. in bar graphs; box-and-whisker plots show quantiles and medians. \* $P<0.05$ , \*\* $P<0.01$ , \*\*\* $P<0.0001$ .

relationships between electrical power and internal impedance during operation (Fig. 4b,  $\mu$ -ILED). The maximum power to the  $\mu$ -ILED results when its impedance finds equilibrium with that of the receiver coil, as observed as the intersection between power-impedance characteristic curves in Fig. 4b. The power from the receiver coil also depends on the RF power applied to the transmission antenna. Figure 4c summarizes the maximum electrical power that can be harvested by HM and BM devices as a function of power to the transmission antenna. The maximum electrical power and corresponding optical irradiance that each blue  $\mu$ -ILED can reach with respect to the power to the transmission antenna for HM and BM devices appears in Fig. 4d. Corresponding thermal powers are in Extended Data Fig. 6a. Similar information for other  $\mu$ -ILEDs are in Extended Data Fig. 6b–e,g,i. The power not consumed by the

$\mu$ -ILEDs can be exploited for the control electronics and for future applications in biosensing or for new illumination schemes that rely on arrays of  $\mu$ -ILEDs.

The optical and thermal power levels described above (Supplementary Table 1) serve as the basis for numerical simulations of the illumination and temperature profiles through adjacent biological tissues, as detailed in the Methods. The transport of light through the brain depends on wavelength-dependent scattering and absorption coefficients and input power, as well as spatial and angular emission profiles. Supplementary Figs. 13 and 14 show the optical-emission and penetration profiles for all wavelengths. Dynamic voltage control further enables users to program the  $\mu$ -ILED optical power and thus the illumination volume and penetration depth. Figure 4e shows this capability as a function of input



optical power of a blue  $\mu$ -ILED. Examples for other  $\mu$ -ILEDs are in Extended Data Fig. 6f,h,j.

Numerical simulations of the temperature distributions in the surrounding brain tissue rely on the thermal power dissipation in the  $\mu$ -ILED (Supplementary Table 1), the optical absorption and the thermal properties of the device and the surrounding biological tissue. Peak temperatures occur at the surface above the  $\mu$ -ILED that directly contacts the brain tissue. Figure 4f shows this temperature increment for a range of irradiances and duty cycles, for a typical stimulation frequency of 20 Hz with a blue  $\mu$ -ILED (additional wavelengths are in Extended Data Fig. 7). The results presented here provide guidelines for choosing  $\mu$ -ILED power and duty cycle for safe operation (see Methods and Supplementary Fig. 15 for details on the simulation model and results).

**Applications of bilateral stimulation and subject-specific programmability for wireless control of place preference and social behavior.** Next, we evaluated the function of the newly developed devices in a series of behavioral assays. Demonstrations of the functionality for the bilateral devices involved experiments on a group of midbrain dopaminergic (DA) neurons in the ventral tegmental area (VTA), a brain region linked to the processing of reward<sup>26,27</sup>. The bilateral design enables surgical implantation of  $\mu$ -ILEDs into the two hemispheres of the brain in a single surgical operation. Stimulation probes with  $\mu$ -ILEDs were positioned posterior to bilateral VTA in DAT<sup>Cre</sup> animals neonatally transduced with Cre-dependent channelrhodopsin (ChR2)-enhanced (E)YFP adeno-associated viral vector (AAV) in midbrain DA neurons (Extended Data Fig. 8a,b). Probe placement and the expression of ChR2-EYFP were verified by histology after behavioral experiments (Extended Data Fig. 8c).

The first test used a well-established paradigm of reward-based behavior, termed real-time place preference. In this paradigm, burst excitation of DA neurons in the VTA and consequent dopamine release promote the animal's preference for the side of the enclosure associated with optogenetic stimulation<sup>8,28</sup> (Extended Data Fig. 8d). Consistent with previous reports<sup>8,28</sup>, burst wireless photostimulation (stim) significantly increased the time animals spent on the stimulated side, in contrast to the absence of place preference in the baseline condition before stimulation (Extended Data Fig. 8e,f). Wireless photostimulation showed no effect on preference in control animals expressing a static fluorophore (Extended Data Fig. 8f). Further tests included the use of bilateral devices in a social-interaction paradigm that involved a choice between a new same-sex conspecific and an inanimate object, as the activation of VTA DA neurons promotes social behavior<sup>20</sup> (Fig. 5a). Compared to baseline and fluorophore controls, time spent in the social-interaction zone ( $14 \times 26 \text{ cm}^2$ ) increased during light stimulation in ChR2-expressing animals, while interaction time with the inanimate object remained unchanged (Fig. 5b,c).

For a direct evaluation of the unique properties of the new-generation wireless optogenetic devices (subject-specific programming and real-time adjustment), we tested the intriguing hypothesis emerging from recent imaging studies<sup>29,30</sup>, which suggests that interbrain neuronal activity synchrony in the medial prefrontal cortex (mPFC) may be sufficient to drive social interactions and social preference within groups of animals. This study is challenging to carry out with traditional optical fibers or large overhead devices, because tangling fibers affect the animals' natural social grooming and other emergent behaviors.

To directly manipulate interbrain activity across subjects, mice were virally transduced with AAV1.CaMKII.ChR2.mCherry in mPFC pyramidal neurons, followed by subsequent implantation of wireless optogenetic devices targeting the mPFC (Fig. 5d). Synchronized interbrain activity was generated using the same stimulation pattern for two mice (5-Hz tonic stimulation), while distinct stimulation patterns (5-Hz tonic versus 25-Hz bursting

stimulation) were used to induce desynchronized activity across animals (Fig. 5e and Supplementary Video 9). We selected 5-Hz stimulation to induce synchronization, based on prior work reporting interbrain synchrony in the theta range as relevant for emergent interactive behaviors<sup>31,32</sup>. The ability of mPFC pyramidal neurons to follow selected stimulation patterns was validated using current-clamp recordings of mPFC neurons in an acute slice preparation, with temporally matched light stimulation using 460-nm whole-field light-emitting diode (LED) illumination (Fig. 5e). We also validated increased excitability in vivo using c-Fos immunofluorescent labeling (Extended Data Fig. 9a–c). Mice receiving in vivo stimulation were allowed to interact with each other freely in an open-field arena ( $18 \text{ cm} \times 25 \text{ cm}^2$ ) (Fig. 5f and Supplementary Video 10), with social and non-social behaviors scored for each subject or pair (Fig. 5g, see Methods for details). The proportion of social behavior in ChR2-expressing mice during synchronized optogenetic stimulation was 46.5% ( $n=12$  pairs), compared to 25.9% during desynchronized stimulation. In fluorophore-expressing control mice ( $n=10$  pairs), the proportion of social behavior was 23.5% for synchronized pairs and 18.4% for desynchronized pairs (Fig. 5h). Figure 5h–j excludes locomotion from analysis to highlight the rarer behavioral events.

For ChR2-expressing mouse pairs, synchronized stimulation increased the amount of time spent engaged in social interaction compared to that with desynchronized stimulation, while the total social-interaction time was not significantly different between two stimulation conditions for fluorophore control mice (Fig. 5i). Among social behaviors, frequencies of affiliative actions of social grooming and sniffing were significantly increased during synchronized stimulation, contributing to the overall greater amount of social-interaction time for ChR2-expressing mouse pairs (Fig. 5j). No significant differences were observed in scored non-social behaviors across all conditions (Fig. 5i,k). Thus, in the context of dyadic social interactions, synchronized stimulation enhances social interaction but not non-social behaviors.

To further evaluate whether interbrain synchrony may shape social preference in more complex social contexts, we leveraged the individualized programmability of NFC-based wireless devices during dynamic social interactions involving three mice at the same time. Two animals were stimulated (tonically) at 5 Hz to form a synchronized pair, while another animal received stimulus-number-matched 25-Hz bursting stimulation, to form an imposed desynchronized pairing with the other two mice (Fig. 5l and Supplementary Video 11). In the fluorophore control mice, we first observed that individuals spent more time engaged in social behaviors in triads, compared to in dyads (Extended Data Fig. 10a). This increase in social interaction in more complex contexts likely reflects both an increase in the amount of time required to process social stimuli associated with multiple individuals and increased density occurring with three mice rather than two mice in the arena of the same size. Evaluating the latter assumption, we simulated the conditions involving interacting dyads and triads in a virtual experimental space ( $18 \times 25 \text{ cm}^2$ , open field). Our modeling result shows that individuals spent more time in proximity to another individual in triads compared to in dyads (Extended Data Fig. 10b), consistent with experimental observations (Extended Data Fig. 10a). We next assessed the distribution of social interaction among the three possible pairs within the triad and found that, for ChR2-expressing triads, more social interactions were observed within the synchronized pair (Fig. 5m and Extended Data Fig. 10c). Focal animals, considered individually, spent more time with their synchronized pair than did fluorophore control animals or more than would be dictated by chance. Animals that could only partake in desynchronized pairs did not distinguish between interaction partners, and their results did not deviate from chance (Fig. 5n). Social-interaction events were more evenly

distributed across animal pairs in fluorophore control animals, and no salient preference was observed for individuals (Fig. 5n and Extended Data Fig. 10c). Non-social behaviors were similar for mice receiving different stimulation patterns in all conditions (Extended Data Fig. 10d).

To determine whether these arbitrarily imposed pairings are stable, we tested whether the optogenetically established social preference can be switched by changing stimulation patterns across pairs in three 10-min-long intervals. At the end of each interval, synchronized stimulation was arbitrarily reassigned to another pair (Extended Data Fig. 10e). During the first period, as described, social preference was established in the synchronized pair, but no new pair preference could be induced during the following session. No significant preference was observed in any fluorophore control pair (Extended Data Fig. 10f). Altogether, these data demonstrate the advantages of NFC-based wireless devices in the study of social behaviors, supporting the hypothesis that imposed interbrain synchrony shapes social interaction and social preference in mice.

## Discussion

Real-time control over optical stimulation patterns is essential for many existing and emerging types of optogenetic studies in free-moving animals and is particularly important for difficult-to-reach brain regions or complex behavioral tasks. The technology presented here employs well-developed NFC power transfer infrastructure and communication protocols that, when aligned with commercial low-cost electronic components and scalable manufacturing techniques, yield a robust and flexible platform well-configured for broad distribution to the community. Recent developments in application-specific integrated circuits offer the opportunity to further integrate this customized multi-component electronic system into a single specialized chip. This approach shares most of the digital and analog operations that this platform supports in the context of user-configurable optogenetic protocols, in a miniaturized form factor<sup>33,34</sup>.

In vivo optogenetic experiments illustrate powerful application opportunities for these devices in behavioral neuroscience research<sup>30</sup>. Our wireless optogenetic platform provides opportunities for unconstrained naturalistic behavioral experiments, especially in the context of social interactions involving multiple free-moving subjects in the same environment. Programmability features enabled by the NFC platform support real-time manipulation of interbrain dynamics in a multi-brain framework experiment. Emerging evidence from multiple human<sup>35–37</sup> and several rodent and bat<sup>29,38</sup> studies suggest that interbrain neural synchrony arising during ongoing social interactions is associated with shared social variables among individuals. We were able to leverage the new NFC-based wireless optogenetic platform to directly test the hypothesis that interbrain synchrony specifically shapes social interactions in pairs or groups of mice. We observed that paired mice display more social behaviors when they received synchronized optogenetic stimulation of mPFC pyramidal neurons at 5 Hz, within the range of the theta band frequency (4–7 Hz) previously reported for interbrain synchronization<sup>30–32</sup>. Moreover, within a group context, social preference arises within pairs that receive synchronized stimulation but not between individuals with a distinct stimulation pattern (5-Hz tonic versus 25-Hz burst stimulation). These results suggest that imposed interbrain synchronization of neural processes can causally shape ongoing social interaction and demonstrate the utility of our system to disentangle complex social phenomena.

Among other applications, next-generation wireless neural devices with added functionalities will continue to deepen our understanding of social behaviors in the multi-brain level framework, potentially providing valuable mechanistic insights into atypical social behaviors (for example, as in autism). A natural extension of this technology available with the current hardware

is the implementation of closed-loop *in vivo* behavioral studies. External events, such as sensor readouts or real-time video feeds, can be used to conditionally trigger the modification of optogenetic stimulation or inhibition protocols in real time using transistor-transistor logic (TTL) pulses, dramatically expanding the space of applications for this technology. In addition, future possibilities enabled by the current advances include multimodal functionality in sensing and other diverse applications.

## Online content

Any methods, additional references, Nature Research reporting summaries, source data, extended data, supplementary information, acknowledgements, peer review information; details of author contributions and competing interests; and statements of data and code availability are available at <https://doi.org/10.1038/s41593-021-00849-x>.

Received: 8 November 2019; Accepted: 26 March 2021;

Published online: 10 May 2021

## References

1. Bassett, D. S. & Sporns, O. Network neuroscience. *Nat. Neurosci.* **20**, 353–364 (2017).
2. Klapoetke, N. C. et al. Independent optical excitation of distinct neural populations. *Nat. Methods* **11**, 338–346 (2014).
3. Boyden, E. S., Zhang, F., Bamberg, E., Nagel, G. & Deisseroth, K. Millisecond-timescale, genetically targeted optical control of neural activity. *Nat. Neurosci.* **8**, 1263–1268 (2005).
4. Deisseroth, K. Optogenetics. *Nat. Methods* **8**, 26–29 (2011).
5. Yizhar, O., Fennel, L. E., Davidson, T. J., Mogri, M. & Deisseroth, K. Optogenetics in neural systems. *Neuron* **71**, 9–34 (2011).
6. Park, S. et al. One-step optogenetics with multifunctional flexible polymer fibers. *Nat. Neurosci.* **20**, 612–619 (2017).
7. Montgomery, K. L. et al. Wirelessly powered, fully internal optogenetics for brain, spinal and peripheral circuits in mice. *Nat. Methods* **12**, 969–974 (2015).
8. Shin, G. et al. Flexible near-field wireless optoelectronics as subdermal implants for broad applications in optogenetics. *Neuron* **93**, 509–521 (2017).
9. Gutruf, P. & Rogers, J. A. Implantable, wireless device platforms for neuroscience research. *Curr. Opin. Neurobiol.* **50**, 42–49 (2017).
10. Gutruf, P. et al. Fully implantable optoelectronic systems for battery-free, multimodal operation in neuroscience research. *Nat. Electron.* **1**, 652–660 (2018).
11. Park, S. I. L. et al. Soft, stretchable, fully implantable miniaturized optoelectronic systems for wireless optogenetics. *Nat. Biotechnol.* **33**, 1280–1286 (2015).
12. Gold, B. T. & Buckner, R. L. Common prefrontal regions coactivate with dissociable posterior regions during controlled semantic and phonological tasks. *Neuron* **35**, 803–812 (2002).
13. Crossley, N. A. et al. Cognitive relevance of the community structure of the human brain functional coactivation network. *Proc. Natl Acad. Sci. USA* **110**, 11583–11588 (2013).
14. Marlin, B. J., Mitre, M., D'Amour, J. A., Chao, M. V. & Froemke, R. C. Oxytocin enables maternal behaviour by balancing cortical inhibition. *Nature* **520**, 499–504 (2015).
15. Capelli, P., Pivetta, C., Soledad Esposito, M. & Arber, S. Locomotor speed control circuits in the caudal brainstem. *Nature* **551**, 373–377 (2017).
16. Hitchcock, P. K., Quinn, J. J. & Taylor, J. R. Bidirectional modulation of goal-directed actions by prefrontal cortical dopamine. *Cereb. Cortex* **17**, 2820–2827 (2007).
17. Tye, K. M. et al. Amygdala circuitry mediating reversible and bidirectional control of anxiety. *Nature* **471**, 358–362 (2011).
18. Ma, T. et al. Bidirectional and long-lasting control of alcohol-seeking behavior by corticostratial LTP and LTD. *Nat. Neurosci.* **21**, 373–383 (2018).
19. Pashaei, R. et al. Optogenetic brain interfaces. *IEEE Rev. Biomed. Eng.* **7**, 3–30 (2014).
20. Gunaydin, L. A. et al. Natural neural projection dynamics underlying social behavior. *Cell* **157**, 1535–1551 (2014).
21. Yizhar, O. Optogenetic insights into social behavior function. *Biol. Psychiatry* **71**, 1075–1080 (2012).
22. Mathis, A. et al. DeepLabCut: markerless pose estimation of user-defined body parts with deep learning. *Nat. Neurosci.* **21**, 1281–1289 (2018).
23. Zhang, Y. et al. Experimental and theoretical studies of serpentine microstructures bonded to prestressed elastomers for stretchable electronics. *Adv. Funct. Mater.* **24**, 2028–2037 (2014).

24. Scott, W. W. *ASM Specialty Handbook: Copper and Copper Alloys* (ASM International, 2001).
25. Lu, L. et al. Wireless optoelectronic photometers for monitoring neuronal dynamics in the deep brain. *Proc. Natl Acad. Sci. USA* **115**, E1374–E1383 (2018).
26. Morales, M. & Margolis, E. B. Ventral tegmental area: cellular heterogeneity, connectivity and behaviour. *Nat. Rev. Neurosci.* **18**, 73–85 (2017).
27. Lammel, S., Lim, B. K. & Malenka, R. C. Reward and aversion in a heterogeneous midbrain dopamine system. *Neuropharmacology* **76**, 351–359 (2014).
28. Tsai, H.-C. et al. Phasic firing in dopaminergic neurons is sufficient for behavioral conditioning. *Science* **324**, 1080–1084 (2009).
29. Kingsbury, L. et al. Correlated neural activity and encoding of behavior across brains of socially interacting animals. *Cell* **178**, 429–446 (2019).
30. Kingsbury, L. & Hong, W. A multi-brain framework for social interaction. *Trends Neurosci.* **43**, 651–666 (2020).
31. Yun, K., Watanabe, K. & Shimojo, S. Interpersonal body and neural synchronization as a marker of implicit social interaction. *Sci. Rep.* **2**, 959 (2012).
32. Toppi, J. et al. Investigating cooperative behavior in ecological settings: an EEG hyperscanning study. *PLoS ONE* **11**, e0154236 (2016).
33. Jia, Y. et al. A mm-sized free-floating wirelessly powered implantable optical stimulation device. *IEEE Trans. Biomed. Circuits Syst.* **13**, 608–618 (2018).
34. Lee, S. Y. et al. 22.7 A programmable wireless EEG monitoring SoC with open/closed-loop optogenetic and electrical stimulation for epilepsy control. In *2019 IEEE International Solid-State Circuits Conference* 372–374 (IEEE, 2019).
35. Montague, P. R. et al. Hyperscanning: simultaneous fMRI during linked social interactions. *Neuroimage* **16**, 1159–1164 (2002).
36. Hasson, U., Ghazanfar, A. A., Galantucci, B., Garrod, S. & Keysers, C. Brain-to-brain coupling: a mechanism for creating and sharing a social world. *Trends Cogn. Sci.* **16**, 114–121 (2012).
37. Liu, T. & Pelowski, M. A new research trend in social neuroscience: towards an interactive-brain neuroscience. *Psych. J.* **3**, 177–188 (2014).
38. Zhang, W. & Yartsey, M. M. Correlated neural activity across the brains of socially interacting bats. *Cell* **178**, 413–428 (2019).

**Publisher's note** Springer Nature remains neutral with regard to jurisdictional claims in published maps and institutional affiliations.

© The Author(s), under exclusive licence to Springer Nature America, Inc. 2021

## Methods

**Fabrication of the flexible circuit and probe.** Patterned laser ablation (ProtoLaser U4, LPKF Laser & Electronics) of a flexible substrate of a copper–PI–copper laminate (18, 75 and 18 µm; DuPont, Pyralux) defined the circuit interconnects, the bonding pads for the electronic components and the geometry of the probe. Flexible printed circuit boards with customized designs can be also obtained from commercial vendors (for example, PCBWay). Conductive pastes (Leitsilber 200 Silver Paint) filled laser-plated via holes through the substrate to electrically connect circuits on the top and bottom sides. Hot-air soldering using low-temperature solder (Indium) bonded packaged components and µ-ILEDs (TR2227, CREE, for emission at 460 nm and 535 nm; TCE12, III–V compounds, for emission at 590 nm and 630 nm) to the respective pads. Chemical vapor deposition (Specialty Coating Systems) formed conformal coatings of parylene (14 µm) to encapsulate the devices. Laser-cut tungsten stiffeners (50 µm, Sigma-Aldrich) were bonded onto the back sides of the probes with a thin layer of epoxy (Devcon) to provide enhanced mechanical rigidity for controlled implantation into the brain. A second layer of parylene (14 µm) and a dip-coated layer of PDMS (Sylgard 184, Dow) completed the formation of a soft encapsulation structure. The BM devices required extra assembly steps before dip coating with PDMS, as described subsequently.

**Fabrication of mechanically compliant interconnects for back subdermal devices.** Fabrication began with spin coating a layer of poly(methyl methacrylate) (3,000 r.p.m., 30 s; PMMA A8, MicroChem) on a silicon wafer substrate. Chemical vapor deposition formed a film of parylene (5 µm) over the PMMA. Electron beam evaporation (AJA International) yielded a multilayer stack of Ti (20 nm), Cu (300 nm), Ti (20 nm) and Au (50 nm), from bottom to top. Photolithography (MLA 150, Heidelberg Instruments) and wet chemical etching defined patterns in this metallic stack in the serpentine geometries of the interconnection traces. Chemical vapor deposition formed a second film of parylene (5 µm) on these patterned metal traces. Sputter deposition (AJA International), photolithography and reactive ion etching (Samco) patterned a layer of SiO<sub>2</sub> (60 nm) as an etch mask. RIE of the exposed parylene defined geometries that matched those of the serpentines, with exposed contact pads for electric connections. The entire structure was transferred from the substrate to water-soluble tape (Aquasol) upon dissolving the PMMA by immersion in acetone. Sputter deposition formed a uniform layer of SiO<sub>2</sub> (30 nm) on the system while on the tape. Exposing the SiO<sub>2</sub> and a thin layer of silicone elastomer (Ecoflex 00-30, Smooth-On) to ultraviolet-induced ozone (UVO-Cleaner Model 144AX, Jelight) created surface hydroxyl termination on both surfaces. Physically laminating the two and then baking at 70 °C for 10 min in a convection oven (Isotemp Microbiological Incubator, Fisherbrand) created a strong adhesive bond. Immersion in warm water dissolved the tape to complete the fabrication process. Several companies can support some of these fabrication steps. For example, Specialty Coating Systems offers chemical vapor deposition of parylene. Thinfilms provides sputter deposition services for thin-metal multilayers and SiO<sub>2</sub>. In addition, most research universities provide microfabrication services to the science community. In this case, photolithography, wet chemical etching and RIE can be made to order.

**Assembly of back-mounted subdermal devices.** Laser ablation of a film of PI (75 µm; Argon Masking) created shadow masks that covered the parylene-encapsulated probes and flexible circuits and left the contact pads for electric connections exposed to allow removal of parylene in these regions by reactive ion etching. Hot-air soldering with a low-temperature solder electrically bonded the probes, interconnection serpentines and flexible circuits. Dip coating with epoxy and PDMS further mechanically secured the joints and encapsulated the probes and flexible circuit. The final step involved encapsulation of the serpentine interconnects with a dip-coated layer of a low-modulus silicone (Ecoflex 00-30).

**Electronic device components.** An RF harvesting module, built with a matching capacitor, high-speed Schottky diodes in a half-cycle regulation configuration and a smoothing capacitor supplied power to the system. The 0201 package configuration for these and other components minimized the overall size. A linear voltage regulator (NCP161, ON Semiconductors, 1 × 1 mm<sup>2</sup>) ensured a constant voltage supply. A low-power, eight-bit microcontroller, (4 × 4 mm<sup>2</sup>, ATtiny84, Atmel) operating with preprogrammed firmware served as the control system. A dynamic NFC-accessible EEPROM (2 × 3 mm<sup>2</sup>, M24LR04E-R, STMicroelectronics) provided external data storage and access by a microcontroller on a write-in-progress event basis to update the device operation. Finally, control of intensity from the µ-ILEDs was implemented with a passive second-order low-pass filter coupled with a high-impedance, ultra-low-power operational amplifier (1.5 × 1.5 mm<sup>2</sup>, TLV8542, Texas Instruments).

**Optical intensity measurement.** An integrating sphere (FOIS-1, Ocean Optics) calibrated with a standard diffusive light source (HL-3 Plus, Ocean Optics) enabled accurate measurements of optical output for all of the µ-ILEDs examined here. A semiconductor device analyzer (Keysight S1500A) supplied current to the µ-ILEDs, from 100 µA to 2 mA with a 100-µA interval, through a probe station (Signatone

1160) during optical measurement. The corresponding software (OceanView, Ocean Optics) generated an output as irradiance flux over the wavelength spectrum from 350 to 1,000 nm. A MATLAB integration script yielded the total optical output power at each current value.

**Mechanical modeling.** The commercial software ABAQUS (ABAQUS Analysis User's Manual 2016) was used to design and optimize the shapes of the serpentine structures and material layouts of the interconnects in multilateral optogenetic devices to improve their mechanical performance and facilitate surgical implantation. For HM devices, PDMS, parylene, copper, PI and tungsten layers were modeled by composite shell elements (S4R). For BM devices, the Ecoflex substrate was modeled by solid hexahedron elements (C3D8R), while other layers were modeled by composite shell elements (S4R), similar to the HM devices. Convergence tests of the mesh size were performed to ensure accuracy. The elastic modulus and Poisson's ratio values used in the simulations were 119 GPa and 0.34 for Cu, 2.1 GPa and 0.34 for parylene, 2.5 GPa and 0.34 for PI, 79 GPa and 0.42 for Au, 110 GPa and 0.34 for Ti and 60 kPa and 0.49 for Ecoflex.

**Electromagnetic modeling.** The commercial software Ansys HFSS (Ansys HFSS 13 User's guide) was used to design and optimize the configuration of the double-loop antenna to achieve relatively large, uniform magnetic fields in the cages for behavior experiments. An adaptive mesh (tetrahedron elements) together with a spherical surface (1,000 mm in radius) as the radiation boundary, was adopted to ensure computational accuracy. The relative permittivity and relative permeability of copper used for the simulations were 1 and 0.999991, respectively. The conductivity of copper used for the simulations was 5.8 × 10<sup>7</sup> S m<sup>-1</sup>.

**Optical and thermal modeling.** The light distribution and temperature change caused by continuous operation of implanted µ-ILEDs was simulated to quantify key functional parameters (that is, penetration depth, illumination volume, temperature change) that describe the physiological interaction with the brain. FEA was implemented with the commercial software COMSOL 5.2a (Equation Based Modeling User's guide) for propagation of light emitted by blue, green, orange and red µ-ILEDs with wavelengths  $\lambda = 460, 535, 590$  and 630 nm, respectively, into mouse brain tissue, according to the Helmholtz equation (equation (1)),

$$\nabla \cdot (-c\nabla\phi) + \mu_a\phi = f \quad (1)$$

where  $\phi$  represents the light fluence rate in the brain,  $c$  is the diffusion coefficient,  $\mu_a$  is the absorption coefficient, and  $f$  is the source term. The isotropic diffusion coefficient can be written as shown in equation (2)<sup>39</sup>,

$$c = \frac{1}{3(\mu_a + \mu'_s)} \quad (2)$$

where  $\mu'_s$  is the reduced scattering coefficient. Absorption and reduced scattering coefficients of the fresh brain, implanted probe materials and µ-ILEDs are given in Supplementary Tables 2 and 3.

For the heat-transfer analysis, FEA was also implemented with the commercial software COMSOL 5.2a (Heat-Transfer Modeling User's Guide) to compute the temperature change ( $\Delta T$ ) caused by the light emitted from the µ-ILEDs, heat generated by thermal power of µ-ILEDs, the brain's metabolism and blood perfusion to account for the physiological heat-transfer phenomenon in the brain. The Pennes' bio-heat equation describes the heat-transfer problem as in equation (3)<sup>40,41</sup>,

$$\rho C_p \frac{\partial T}{\partial t} + \nabla \cdot (-k\nabla T) = \rho_b C_b \omega_b (T_b - T) + Q_{\text{met}} + Q_{\text{the}} + \phi\mu_a \quad (3)$$

where  $T$  is temperature,  $t$  is time;  $k$ ,  $\rho$  and  $C_p$  are the thermal conductivity, mass density and heat capacity of the brain, and  $\rho_b$  and  $C_b$  are the mass density and specific heat capacity of the blood, respectively.  $\omega_b$  denotes the blood perfusion rate<sup>40</sup> and  $T_b$  is the arterial blood temperature<sup>40</sup>.  $Q_{\text{met}}$  is the heat source from metabolism in the brain,  $Q_{\text{the}}$  is the heat generated by thermal power of µ-ILEDs, and  $\phi$  corresponds to the light fluence rate of the µ-ILEDs calculated in the optical simulation. The thermal properties of the implanted probe and bio-heat input parameters used in the simulation are given in Supplementary Tables 4 and 5.

The brain tissue, implanted probe geometry and the µ-ILEDs were modeled using four-node tetrahedral elements. Convergence tests of the mesh size were performed to ensure accuracy. The total number of elements in the models was approximately 905,000.

**In vivo studies. Animals.** All experiments used young adult male wild-type C57BL/6J mice (6–12 weeks old and weighing 20–30 g at the start of experiments; Jackson Laboratory), maintained at ~25 °C with humidity ranging from 30% to 70%. Mice were maintained on a 12-h-light–dark cycle (lights on at 9:00 PM, reverse light cycle) and fed ad libitum. Mice were group housed (two to four per cage) before surgery, after which mice were individually housed in a climate-controlled vivarium. All experimental procedures were conducted

in accordance with the National Institutes of Health standards and were approved by the Institutional Animal Care and Use Committees of the US Army Medical Research Institute of Chemical Defense, Northwestern University and Washington University.

**Surgical procedures.** Animals were anesthetized using isoflurane and their head and back fur was shaved. Mice were then mounted in a stereotactic frame with a heating pad, and an incision was made down the center of the scalp to expose the skull. Burr holes for implantation of optogenetic probes were drilled in the skull using a variable-speed surgical drill. Using the attachment flag, optogenetic probes were stereotactically lowered into the designated brain region at a rate of  $\sim 100 \mu\text{m s}^{-1}$  until appropriately positioned. The probes were then affixed to the skull using cyanoacrylate to prevent further movement. For BM devices, a second  $\sim 10\text{-mm}$  incision was made midway down and across the back. The subcutaneous fascia between the scalp and back incision were separated, and the wireless device was then pulled from the scalp incision posteriorly until it rested above the spine. Serpentine wires connecting the two optogenetic probes to the thin and flexible wireless antenna traveled subcutaneously through the neck to connect the two components. The incisions were sutured closed, and animals were monitored and allowed to recover for several hours before transfer back to the cage area facility for appropriate post-surgical monitoring.

DAT<sup>Cre/+</sup> neonates (P3–P6) were transduced with AAV1.EF1 $\alpha$ .DIO.hChR2(H134R).EYFP ( $3.55 \times 10^{13}$  genome copies (GC) per ml), (Addgene, viral preparation 20297/20298-AAV1, K. Deisseroth, Stanford University) or AAV8-CAG-FLEX-GFP ( $3.1 \times 10^{12}$  GC ml $^{-1}$ , UNC Vector Core, E. Boyden, Massachusetts Institute of Technology). Six weeks after viral transduction, wireless probes were positioned posterior to the VTA (referenced from the bregma,  $-3.1\text{ mm anteroposterior}, \pm 0.5\text{ mm medio-lateral and } -4.7\text{ mm dorsoventral}$ ). C57BL/6 mice ( $\sim P60$ ) were transduced with AAV1.CaMKIIa.hChR2(H134R).mCherry ( $1.2 \times 10^{13}$  GC ml $^{-1}$ , Addgene, viral preparation 26975-AAV1, K. Deisseroth). Two weeks after viral transduction, wireless probes were positioned anterior to the mPFC (referenced from the bregma,  $+2.2\text{ mm anteroposterior}, +0.5\text{ mm medio-lateral and } -1.5\text{ to } 2.0\text{ mm dorsoventral}$ ). Mice recovered for at least 5 d before behavioral experiments.

**Histology.** For hematoxylin and eosin staining, standard protocols were followed. Four- $\mu\text{m}$ -thick tissue sections adhered to slides were dewaxed and cleared with xylene, hydrated by incubation in a series of decreasing concentrations of alcohols (100–70%), stained with filtered hematoxylin, treated with an alkaline solution and counterstained with eosin. Subsequently, sections were dehydrated in several changes of alcohol, cleared and coverslipped. Sections were imaged using an Olympus VS120 microscope in bright-field mode. Colored bright-field images of back tissue sections were automatically acquired and stitched by using an automated slide scanner and a  $\times 40$  objective.

For immunofluorescent c-Fos labeling, 50–80  $\mu\text{m}$ -thick sections were incubated with the primary rabbit anti-c-Fos antibody in 0.5% Triton X-100 PBS overnight at 4 °C (1:10,000, 226003, Synaptic Systems). For evaluation of biocompatibility, rabbit anti-GFAP (1:1,000, ab7260, Abcam), rabbit anti-IBA1 (1:1,000, ab178846, Abcam) and rabbit anti-hemoglobin subunit  $\alpha$  (1:500, ab92492, Abcam) antibodies were used. On the following day, tissues were rinsed three times with PBS, reacted with anti-rabbit Alexa Fluor 647 secondary antibody (1:500, Thermo Fisher) for 2 h at room temperature and rinsed again three times with PBS. Sections were mounted on Superfrost Plus slides (Thermo Fisher), air dried and coverslipped under glycerol:TBS (9:1) with Hoechst 33342 (2.5  $\mu\text{g ml}^{-1}$ , Thermo Fisher Scientific). For c-Fos quantification,  $\sim 30\text{-}\mu\text{m}$  stacks with a step size of 2  $\mu\text{m}$  were acquired with a Leica SP5 confocal microscope for the following regions, including the ipsilateral mPFC, contralateral mPFC and ipsilateral M1. All imaging parameters were constant across all samples, and each channel was imaged sequentially with a  $\times 40$  objective. Analysis was carried out in Fiji<sup>42</sup> using autothresholding and particle-analysis scripts. The same analysis parameters were applied across all regions of interest.

**Electrophysiology.** Coronal brain slice preparation was modified from previously published procedures<sup>43–45</sup>. Animals were deeply anesthetized by inhalation of isoflurane, followed by a transcardial perfusion with ice-cold, oxygenated artificial cerebrospinal fluid (ACSF) containing (in mM) 127 NaCl, 2.5 KCl, 25 NaHCO<sub>3</sub>, 1.25 NaH<sub>2</sub>PO<sub>4</sub>, 2.0 CaCl<sub>2</sub>, 1.0 MgCl<sub>2</sub> and 25 glucose (osmolarity, 310 mOsm l $^{-1}$ ). After perfusion, the brain was rapidly removed and immersed in ice-cold ACSF equilibrated with 95% O<sub>2</sub>–5% CO<sub>2</sub>. Tissue was blocked and transferred to a slicing chamber containing ice-cold ACSF, supported by a small block of 4% agar (Sigma-Aldrich). Bilateral 250- $\mu\text{m}$ -thick mPFC slices were cut on a Leica VT1000S (Leica Biosystems) in a rostro-caudal direction and transferred into a holding chamber with ACSF, equilibrated with 95% O<sub>2</sub>–5% CO<sub>2</sub>. Slices were incubated at 34 °C for 30 min before electrophysiological recording. Slices were transferred to a recording chamber perfused with oxygenated ACSF at a flow rate of 2–4 ml min $^{-1}$  at room temperature.

Current-clamp whole-cell recordings were obtained from neurons visualized under infrared DIC contrast video microscopy using patch pipettes with resistance of  $\sim 2\text{--}5\text{ M}\Omega$ . mPFC neurons expressing ChR2 were identified by the expression

of mCherry. To activate ChR2-expressing pyramidal neurons in the mPFC, tonic light pulses at 5 Hz or bursting light pulses at 25 Hz (1-s-long burst every 5 s) were delivered at the recording site using whole-field illumination through a  $\times 60$  water-immersion objective (Olympus) with a pE-4000 CoolLED illumination system (CoolLED). Recording electrodes contained the following (in mM): 135 K gluconate, 4 KCl, 10 HEPES, 10 Na phosphocreatine, 4 MgATP, 0.4 Na<sub>2</sub>GTP and 1 EGTA (pH 7.2, 295 mOsm l $^{-1}$ ). Recordings were made using 700B amplifiers (Axon Instruments); data were sampled at 10 kHz and filtered at 4 kHz with a MATLAB-based acquisition script (MathWorks).

**Experimental setup for behavioral studies.** A host computer supports a customized GUI, developed in MATLAB and connected to the RF power module and the NFC reader that operates the ISO 15693 NFC communication protocol (LRM2500-A, Feig Electronics). The computer connects to the RF power module via RS232 serial communication (an RS232-to-USB converter was used to compensate for the lack of physical RS232 ports in modern computers). The power module (Neurolux) drives a dual-loop antenna that wraps around the experimental enclosure. An antenna tuner (Neurolux) provides impedance matching between the RF power module and the antenna to efficiently transmit power and communication signaling. The customized GUI controls the information flow via write-read commands to NFC optogenetic devices via the NFC reader. Up to four devices can be addressed independently using their unique device identifier codes. A straightforward modification to the GUI can support additional devices. The write-read commands allow modification of illumination parameters, activation or deactivation of the  $\mu$ -ILEDs or activation of two devices simultaneously. In addition, this interface permits control of the RF module such as the power output. Although not implemented here, further on-demand activation of a target device via external signal controls such as TTL represents a natural extension of this system.

**Real-time place preference.** Mice were placed in a custom two-compartment conditioning apparatus ( $61 \times 30.5 \times 30.5\text{ cm}^3$ ) as described previously<sup>8,28</sup>. Mice underwent a 20-min trial in which entry into one compartment triggered a burst of wirelessly powered photostimulation for 300 ms at 30 Hz (5-ms pulse width). Burst stimulations were delivered every 5 s while a mouse remained in the stimulation-paired chamber. Departure from the stimulation-paired side and entry into the other chamber side resulted in the cessation of photostimulation. The stimulation side was decorated with a vertical grating pattern, and the no-stimulation side was decorated with horizontal gratings. Mice were excluded from the study if they showed preference for either side in the baseline condition without photostimulation. The video recorded in each session was analyzed by ToxTrac<sup>46</sup>. Time spent on each side was quantified as a measurement of place preference. Data were analyzed blind to conditions.

**Social preference with DA stimulation.** Mice underwent the social-interaction test during a 5-min episode. A new same-sex mouse was placed in a plastic mesh cage ( $10 \times 6\text{ cm}^2$ ) on one side of the open field ( $44 \times 44\text{ cm}^2$ ). A mouse-shaped object was placed on the opposite side. The experimental mouse was allowed to freely explore the open field for 2 min before a new mouse and object were placed into the arena. Videos analyzed by ToxTrac<sup>46</sup> were used to measure the amount of time the experimental mouse spent in the ‘interaction zone’ ( $14 \times 26\text{ cm}^2$  around the center of the mesh cage or object). One day following a baseline session without stimulation, burst light stimulation (300-ms burst every 3 s, nine pulses at 30 Hz in each burst, 5-ms pulse width) was delivered during the test period, and the interaction times with the new mouse and the inanimate object were measured. Data were analyzed blind to conditions.

**Social interaction and preference with interbrain synchrony.** In paired-mice social-interaction experiments, two male mice implanted with wireless optogenetic devices were placed in an open-field arena ( $18 \times 25\text{ cm}^2$ ) for free social interaction. For paired-mice social-interaction experiments, pairs received synchronized or desynchronized stimulation for a 5-min period. During the synchronized session, two mice were simultaneously stimulated at 5 Hz (5-ms pulse width). During the desynchronized session, one mouse was stimulated at 5 Hz, while the other mouse received bursting optogenetic stimulation (1-s burst every 5 s, 25 pulses at 25 Hz in each burst, 5-ms pulse width). The order of synchronized and desynchronized sessions was randomized for pairs. All animals were habituated to the open-field arena for 5 min before testing. For triple-mice social preference, each experiment consisted of three sequential sessions (10 min each). During each session, two mice were simultaneously stimulated at 5 Hz, and the third mouse received bursting stimulation at 25 Hz. At the end of each session, stimulation patterns and the synchronized pair were reassigned.

The videos, recorded at 25 fps, were analyzed by Behavioral Observation Research Interactive Software<sup>47</sup>. Behaviors were manually scored for individual animals or pairs, as noted in the results and figures. Investigators were not blinded to the stimulation patterns displayed by the indicator LEDs. Behavioral events were converted into binary vectors for each type of behavior using 1-s bins to generate behavioral sequences. A total of nine social and non-social behaviors were quantified. Social behaviors included all grooming, approach, pursue, sniff, attack

and escape. Non-social behaviors included self-groom, dig and rear. Total time spent engaged in social interaction and non-social behaviors was calculated for comparisons among conditions.

**Simulation of subject proximity.** Mice were modeled as ellipses with a 60-mm major axis and a 30-mm minor axis. Their movement was simulated in a  $25 \times 18 \text{ cm}^2$  arena. For each movement, each object's speed was sampled from a Gaussian distribution with a mean of  $0.09 \text{ mm ms}^{-1}$  and a standard deviation of  $0.06 \text{ mm ms}^{-1}$ , matching the distribution of reported mouse speeds<sup>48</sup>. Movement duration was chosen to be on average one fifth of body length, fixed at 133.33 ms. The simulated objects were initially placed equidistantly across the arena width, at half the arena height. The first movement direction was sampled from a uniform distribution over  $0, 2\pi$ . Each subsequent movement was sampled from a Gaussian distribution centered at the object's previous heading direction with a standard deviation of  $\pi/4$ . If the object encountered a wall, its movement direction was then sampled from a uniform distribution over  $0, 2\pi$ . Objects were not allowed to overlap. Objects were considered interacting if their perimeters were  $<3 \text{ mm}$  from each other.

**Microscale computed tomography imaging.** Animals were anesthetized with isoflurane and placed inside a preclinical microPET/CT imaging system (Mediso nanoScan scanner). Data were acquired with 'medium' magnification, a  $33\text{-}\mu\text{m}$  focal spot and  $1 \times 1$  binning, with 720 projection views over a full circle, with a 300-ms exposure time. Three images were acquired, using 35 kVp, 50 kVp and 70 kVp (where kVp is peak kilovoltage). Projection data were reconstructed with a voxel size of  $34 \text{ }\mu\text{m}$  using filtered (Butterworth filter) back-projection software from Mediso Nucline (version 2.01). Throughout imaging, respiratory signals were monitored using a digital system developed by Mediso. Advanced imaging studies used five C57BL/6 mice weighing 25–30 g (C57BL/6NCrl) and three Sprague Dawley rats weighing 250–300 g from Charles River. In mice, the VTA was targeted for probe placement (referenced from the bregma,  $-3.3 \text{ mm}$  anteroposterior,  $\pm 0.5 \text{ mm}$  medio-lateral and  $-4.4 \text{ mm}$  dorsoventral). In the rats, probes were placed  $-5.0 \text{ mm}$  anteroposterior,  $\pm 2.4 \text{ mm}$  medio-lateral and  $-5.0 \text{ mm}$  dorsoventral. Data were analyzed with Amira (version 2020.2, Thermo Fisher Scientific). Bone density was calculated from mean (Hu) values acquired with 50 kVp.

**Mobility studies. Stereotaxic surgery.** Mice were anesthetized in an induction chamber (3% isoflurane) and then placed in a stereotaxic frame (Kopf) where they were maintained at 1–2% isoflurane. All surgeries were performed using aseptic conditions. Meloxicam ( $0.5 \text{ mg ml}^{-1}$ , subcutaneous injection) and lidocaine (0.25–0.5%, intradermal injection) were given as preoperative analgesia. After a stable plane of anesthesia was reached, a midline incision was made to expose the skull. Two burr holes were drilled at the site of viral injection (all groups) and probe placement (for tethered and wireless subjects). Surgical controls only received viral injections; no probes were implanted. All mice were injected bilaterally with 200 nl per side of AAV-CaMKIIα-hChR2-EYFP (UNC Vector Core, K. Deisseroth) at a rate of  $100 \text{ nl min}^{-1}$  via microsyringe pump (UMP3, WPI) and controller (Micro4, WPI). After 5 min, the injection needles ( $10 \mu\text{l}$  NanoFil with 33-gauge needles, WPI) were raised  $300 \mu\text{m}$  and left in place for an additional 3 min to allow for diffusion of the virus throughout the tissue. Mice were then implanted bilaterally with fiber-optic ferrules (1.25 mm, stainless steel, Thorlabs) that contained the implanted optical multimode fibers ( $200 \mu\text{m}$ , 0.22 NA, Thorlabs) or wireless μ-ILED optogenetic probes using a stereotaxic holder (PH-300, ASI Scientific) and affixed with dental cement (fibers) or cyanoacrylate (wireless). Mice were allowed to recover for 2.5 weeks before acclimation to tethering and/or handling began. All animals gained weight after the surgery and readily built nests in their new cages.

**Open-field test.** To perform the open-field analysis for sham and HM-device-implanted mice, we used a  $42 \times 42 \times 20 \text{ cm}^3$  (length  $\times$  width  $\times$  height) open arena. Animals were placed in the center of the arena and allowed to freely explore the open-field enclosure for 15 min, under low-light conditions (50 lx), while they were recorded with an overhead camera. Digital recordings were collected and analyzed using ANY-maze video tracking software, measuring the total distance and average speed, in addition to the time and distance traveled in both the inner and outer zones. The center zone was defined as a square comprising 50% of the arena.

The new open-field tests for sham, fiber-implanted and BM-device-implanted mice were carried out during the more active dark cycle (9:00 AM–9:00 PM) between 10:00 AM and 11:00 AM in a sound-attenuated lab maintained at 23 °C. All tests were performed in a  $908\text{-cm}^2$  (34 cm in diameter) circular cage that was new for the animals to encourage exploratory activity and maximize movement. For fiber-optogenetic-probe tethering, a  $1 \times 2$  step-index multimode fiber-optic coupler (105  $\mu\text{m}$ , 0.22 NA, Thorlabs) was connected to a low-torque hybrid rotary joint (0.22 NA, Doric Lenses) and to the bilateral implanted ferrules in the mouse skull. No extra connections were required for mice implanted with wireless probes or the surgical controls. All mice were gently handled for 3 d before behavioral tests to acclimate the subjects to the experimenter and to reduce stress. Additionally, fiber-implanted mice were habituated to fiber-optic tethering in their home cages for 3 d before behavioral experiments to prevent acute stress from interfering with

their behavior on test days. For testing, mice ( $n=6$ –8 per group) were placed in the center of the open field and allowed to roam freely for 1 h. Movements were recorded by video, and motion analysis was performed offline using EthoVision 11 software. Distance traveled, velocity and number of stops and starts were calculated in 1- and 5-min bins for the duration of the recording and statistically compared among groups using ANOVA.

**Running wheel.** Similar to the open-field tests, these experiments were carried out during the more active dark cycle to promote higher activity. Animals were placed in a circular cage containing a Med Associates Low-Profile Running Wheel that measures revolutions per minute of running activity. All animals had access to running wheel enrichment devices in their home cages to acclimate them to the device before recording. Animals were run for 3 consecutive days to further promote consistent activity and minimize potential negative effects from acute tethering of the fiber-optic group. Data reported are from the third day of recording using time bins from 5 to 65 min.

**Positional tracking of mice.** Tracking the position of four body parts of a mouse during natural behaviors provided estimates for the requirements on mechanical deformations of soft interconnects mounted subdermally on the back. The procedure used a mouse in a transparent chamber ( $30 \text{ cm} \times 30 \text{ cm}$ ), recorded from one side for 1 h (Raspberry Pi, 25 frames per second). Tracking information was determined using DeepLabCut<sup>22</sup>. Manually marking four body parts (head, neck, back and tail) in 200 representative frames generated a training set for a convolutional neural network designed to locate these four body parts on a frame-by-frame basis. A subset of frames (~9,000) with the animal's major axis oriented perpendicular to the camera were used to compute the deformation of the body regions. Estimates of mechanical compression and stretching used the combined distance from head to neck and neck to back. The bending curvature was represented as the radius of the arc formed by the points of head, neck and back. All data points were compared to the medians of the dataset (referenced as the non-deformed state) to indicate the level of device deformation during natural activity.

**Statistical analyses.** Group statistical analyses were performed using GraphPad Prism 7 software (GraphPad). For  $n$  sizes, the number of animals is provided. No statistical methods were used to predetermine sample sizes, but our sample sizes are similar to those reported in previous publications<sup>8,29,45</sup>. All samples were randomly assigned to experimental groups. Data from failed devices were excluded from the analysis. All data are expressed as mean  $\pm$  s.e.m. or as individual plots. Data distribution was assumed to be normal, but this was not formally tested. For two-group comparisons, statistical significance was determined by two-tailed Student's *t*-tests. For multiple-group comparisons, ANOVA tests were used, followed by post hoc analyses.  $P < 0.05$  was considered statistically significant.

**Reporting Summary.** Further information on experimental design and reagents is available in the Nature Research Life Sciences Reporting Summary linked to this paper.

## Data availability

Raw data generated during the current study are available from the corresponding author on reasonable request. The data analyzed during the current study are available at [https://github.com/A-VazquezGuardado/Real-time\\_control\\_Optogenetics](https://github.com/A-VazquezGuardado/Real-time_control_Optogenetics). Source data are provided with this paper.

## Code availability

All computer code and customized software generated during and/or used in the current study are available at [https://github.com/A-VazquezGuardado/Real-time\\_control\\_Optogenetics](https://github.com/A-VazquezGuardado/Real-time_control_Optogenetics).

## References

39. Bazrafkan, S. & Kazemi, K. Modeling time resolved light propagation inside a realistic human head model. *J. Biomed. Phys. Eng.* **4**, 49–60 (2014).
40. Stujenske, J. M., Spellman, T. & Gordon, J. A. Modeling the spatiotemporal dynamics of light and heat propagation for in vivo optogenetics. *Cell Rep.* **12**, 525–534 (2015).
41. Aronov, D. & Fee, M. S. Analyzing the dynamics of brain circuits with temperature: design and implementation of a miniature thermoelectric device. *J. Neurosci. Methods* **197**, 32–47 (2011).
42. Schindelin, J. et al. Fiji: an open-source platform for biological-image analysis. *Nat. Methods* **9**, 676–682 (2012).
43. Xiao, L., Priest, M. F., Nasenbeny, J., Lu, T. & Kozorovitskiy, Y. Biased oxytocinergic modulation of midbrain dopamine systems. *Neuron* **95**, 368–384 (2017).
44. Xiao, L., Priest, M. F. & Kozorovitskiy, Y. Oxytocin functions as a spatiotemporal filter for excitatory synaptic inputs to VTA dopamine neurons. *eLife* **7**, e33892 (2018).

45. Wu, M., Minkowicz, S., Dumrongprechachan, V., Hamilton, P. & Kozorovitskiy, Y. Ketamine rapidly enhances glutamate-evoked dendritic spinogenesis in medial prefrontal cortex through dopaminergic mechanisms. *Biol. Psychiatry* <https://doi.org/10.1016/j.biopsych.2020.12.022> (2021).
46. Rodriguez, A. et al. ToxTrac: a fast and robust software for tracking organisms. *Methods Ecol. Evol.* **9**, 460–464 (2018).
47. Friard, O. & Gamba, M. BORIS: a free, versatile open-source event-logging software for video/audio coding and live observations. *Methods Ecol. Evol.* **7**, 1325–1330 (2016).
48. Broom, L. et al. A translational approach to capture gait signatures of neurological disorders in mice and humans. *Sci. Rep.* **7**, 3225 (2017).

## Acknowledgements

This work used the Northwestern University Micro/Nano Fabrication Facility, which is partially supported by the Soft and Hybrid Nanotechnology Experimental Resource (NSF ECCS-1542205), the Materials Research Science and Engineering Center (DMR-1720139), the State of Illinois and Northwestern University. This work was funded by NINDS R01NS106953 to R.W.G. and the Medical Scientist Training Program grant T32GM07200 and NINDS NRSA 5F31NS103472-02 to J.G.G.-R. Surgical and imaging work was performed by the Developmental Therapeutics Core and the Center for Advanced Molecular Imaging at Northwestern University, which are generously supported by NCI CCSG P30 CA060553 awarded to the Robert H. Lurie Comprehensive Cancer Center. Histology services were provided by the Northwestern University Mouse Histology and Phenotyping Laboratory, which is supported by NCI P30 CA060553 awarded to the Robert H. Lurie Comprehensive Cancer Center. From the US Army Medical Research Institute of Chemical Defense, we thank J. Abraham for his assistance with graphics, T. Shih for sharing his laboratory space and A. Collazo Martinez for laboratory support. C.H.G. is supported by the LUCI program, sponsored by the Basic Research Office, Office of Under Secretary of Defense for Research and Engineering. Y.K. is supported by the NIH (R01MH117111 and R01NS107539), a Rita Allen Foundation Scholar Award, the Searle Scholar Award and a Beckman Young Investigator Award. M.W. is supported as an affiliate fellow of the NIH (T32 AG20506), and S. Minkowicz is supported by the NSF GRFP (DGE-1842165). V.D. is a predoctoral fellow of the American Heart Association (19PRE34380056). Z.R.D. is supported by NIH DP2OD026143, a Whitehall Foundation grant and the Dana Foundation. Z.X.

acknowledges support from the National Natural Science Foundation of China (grant no. 12072057) and Fundamental Research Funds for the Central Universities (grant no. DUT20RC(3)032). Y.H. acknowledges support from the NSF (CMMI1635443).

## Author contributions

Y. Yang, Z.X., M.W., A.V.-G., R.W.G., C.H.G., Z.R.D., Y.H., Y.K. and J.A.R. contributed ideas and designed research. Y. Yang, Z.X., C.H.G. and J.A.R. proposed the platform design. Z.X., Y.D., R.A., S.Z. and Y.H. conducted structural optimization and performed electromagnetic, optical and thermal modeling and analysis. M.W., S. Minkowicz, V.D., Z.R.D. and Y.K. designed, carried out and analyzed optogenetic studies and body-motion tests. A.V.-G. and Y. Yang established the electronic system. A.J.W., J.G.G.-R., M.W., J.A.M., R.W.G. and C.H.G. developed implantation processes. A.J.W., J.G.G.-R., J.A.M. and C.H.G. conducted mobility studies. Y. Yang, M.W., A.V.-G., Z.X., A.J.W., J.G.G.-R., Y.D., T.W., R.A., J.A.M., S. Minkowicz, V.D., J.L., S.Z., A.A.L., Y.M., S. Mehta, D.F., L.H., W.B., M.H., H.Z., W.L., Y. Yu, X.S., A.B., X.Y. and C.H.G. performed experiments. Y. Yang, M.W., Z.X., A.V.-G., A.J.W., J.G.G.-R., Z.R.D., Y.K. and C.H.G. analyzed data. Y. Yang, Z.X., M.W., A.V.-G., A.J.W., C.H.G., Z.R.D., Y.H., Y.K. and J.A.R. wrote the paper with input from other authors.

## Competing interests

R.W.G., A.B. and J.A.R. are cofounders in a company, Neurolux, Inc., that offers related technology products to the neuroscience community.

## Additional information

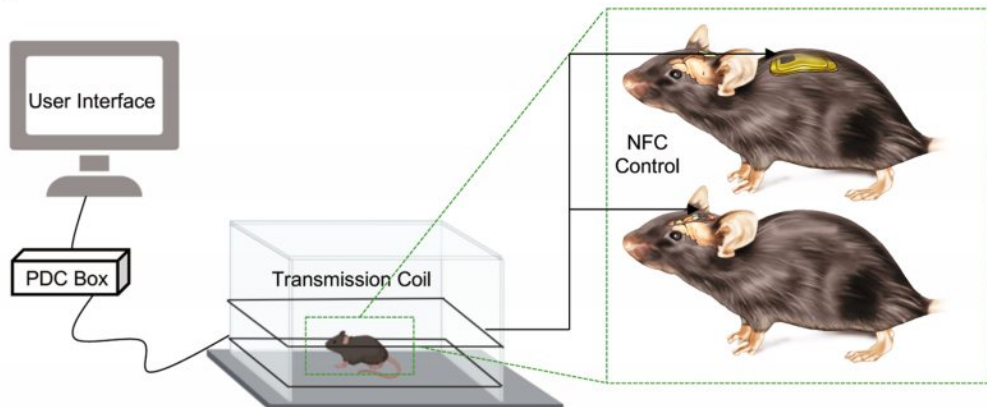
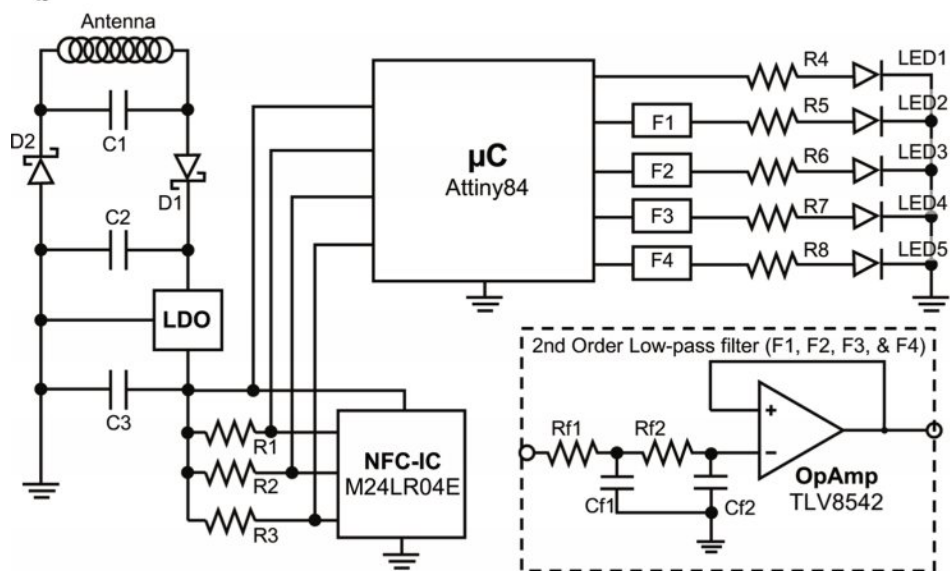
**Extended data** is available for this paper at <https://doi.org/10.1038/s41593-021-00849-x>.

**Supplementary information** The online version contains supplementary material available at <https://doi.org/10.1038/s41593-021-00849-x>.

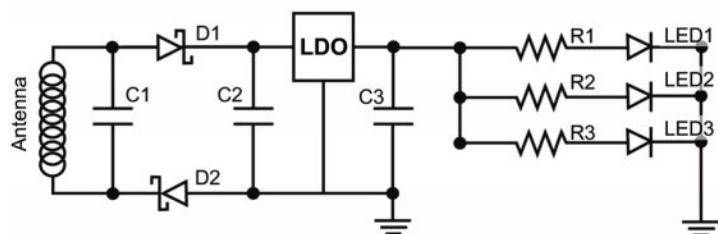
**Correspondence and requests for materials** should be addressed to Z.X., Y.H., Y.K. or J.A.R.

**Peer review information** *Nature Neuroscience* thanks Avishek Adhikari, Ada Poon, and the other, anonymous, reviewer(s) for their contribution to the peer review of this work.

**Reprints and permissions information** is available at [www.nature.com/reprints](http://www.nature.com/reprints).

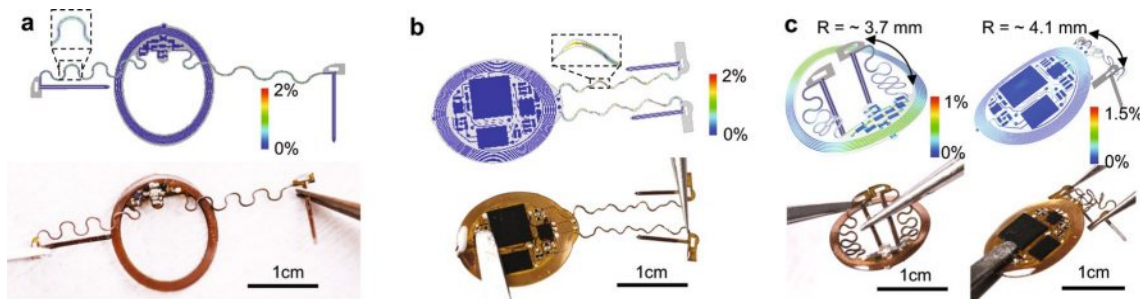
**a****b**

Component	Description/Value
C1	Varies (18pF)
C2	2.2 $\mu$ F
C3	1.0 $\mu$ F
Cf1	22 pF
Cf2	22 pF
D1, D2	Schottky diodes
LDO	Varies
R1, R2, and R3	4.7 k $\Omega$
R4	1.0 k $\Omega$
R5	Varies
R6	Varies
R7	Varies
R8	Varies
Rf1, Rf2	10 M $\Omega$

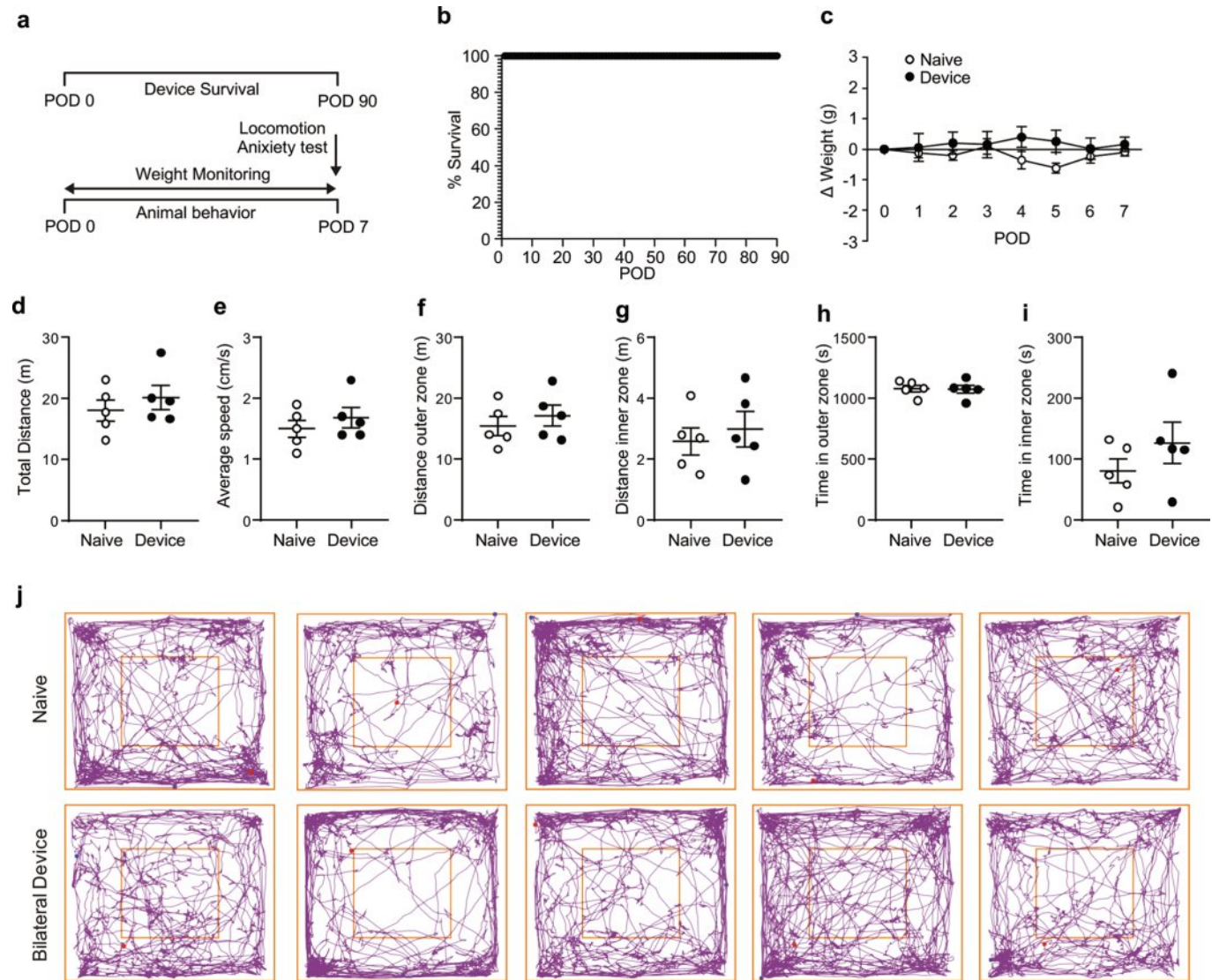
**c**

Component	Description/Value
C1	Varies (18pF)
C2	2.2 $\mu$ F
C3	1.0 $\mu$ F
D1, D2	Schottky diodes
LDO	Varies
R1	Varies
R2	Varies
R3	Varies

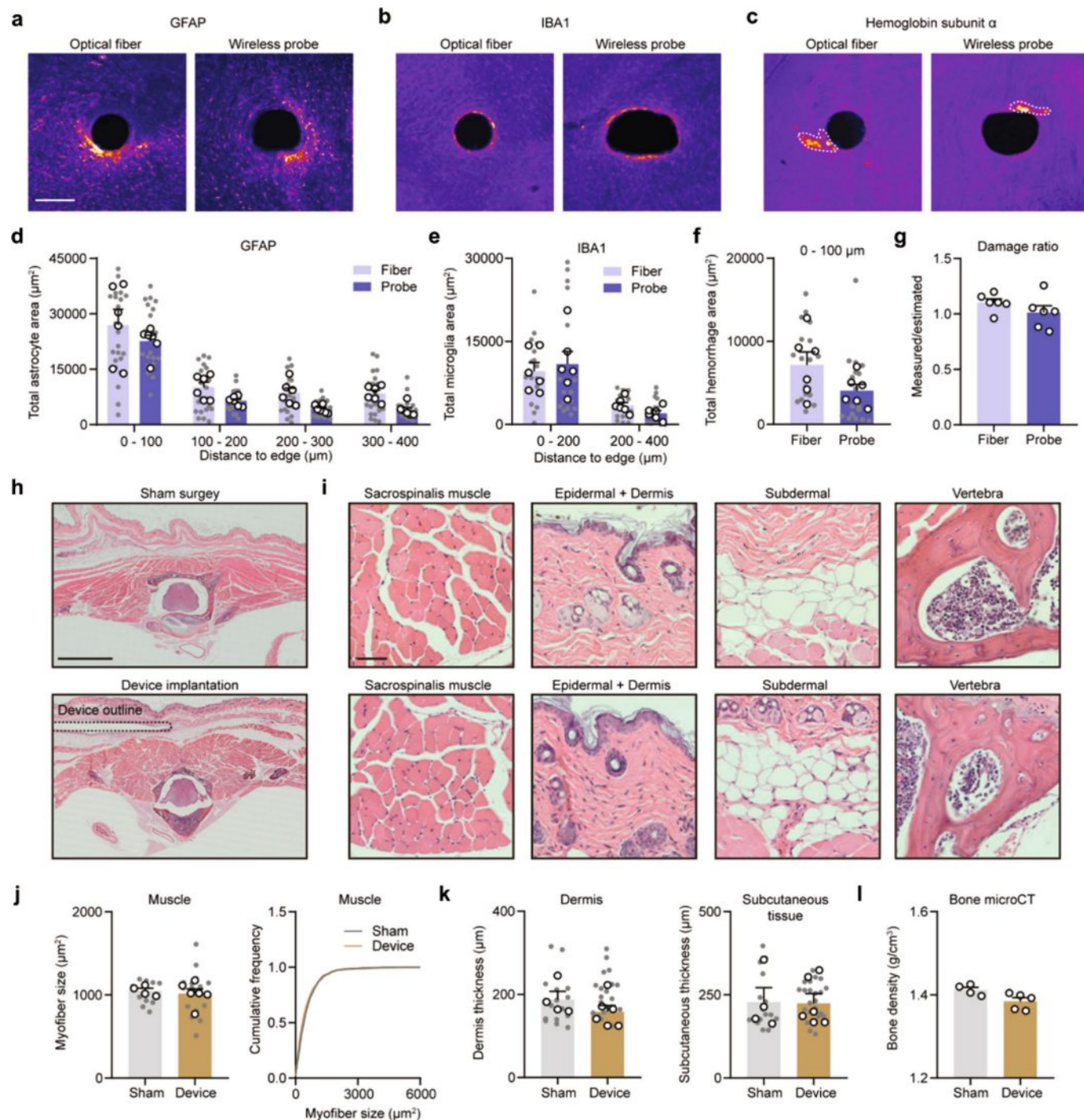
**Extended Data Fig. 1 | Electrical circuit implemented in the NFC-enabled platform.** **a**, The experimental platform includes the implanted device, transmission antenna, power distribution (PDC) box, and PC with user interface. The device is wirelessly programmed using a PC in a real-time manner through near field communication (NFC) control over the stimulation parameters. **b**, The NFC corresponds to an RF addressable memory chip supporting ISO15693 protocol. The microcontroller interfaces to the NFC memory via the I2C communication protocol. Up to four channels are supported by the microcontroller's firmware, independently controlled by the end user. Each channel is filtered using a second order low-pass passive filter whose output is coupled by a high impedance voltage follower that drives the  $\mu$ -ILED. The number of channels to be used depends on the type of implant: two for head mounted devices or four for back mounted devices. **c**, Simple voltage regulation circuit that implements a low dropout regulator (LDO) that passes current directly to the  $\mu$ -ILEDs and resistor after rectification. The component bill of materials is also shown.



**Extended Data Fig. 2 | Mechanical deformations for head mounted devices.** **a, b**, FEA simulations and photographs of 30% stretching of different head mounted devices. **c**, FEA simulations and photographs of these devices deformed into various configurations after implantation.

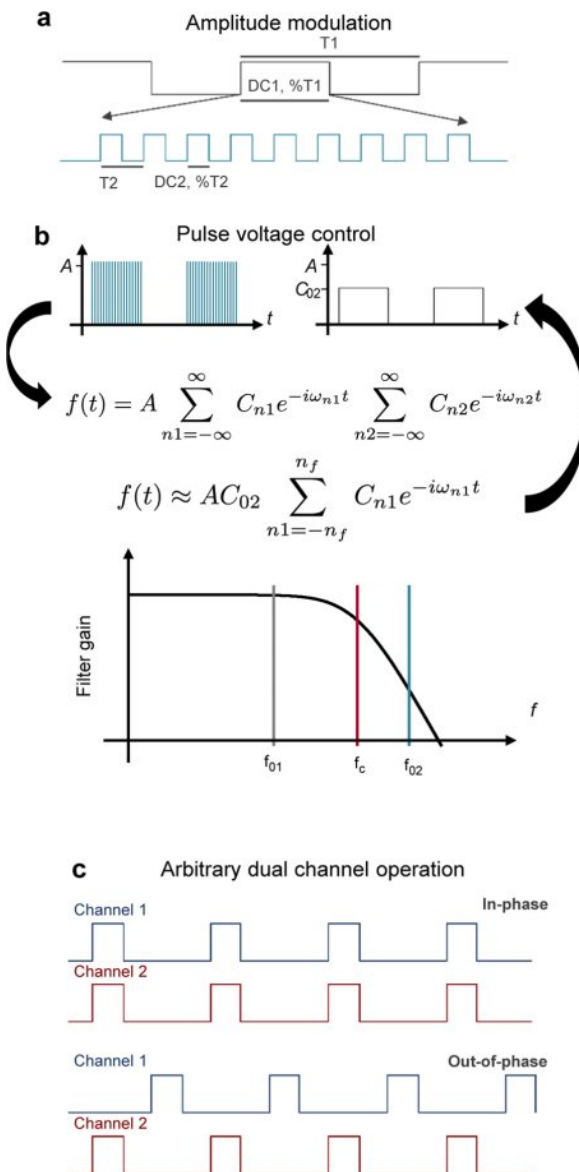


**Extended Data Fig. 3 | Device longevity and behavioral outcomes for head mounted devices.** **a**, Cartoon representation of the timeline for monitoring device longevity and animal postoperative behavior. **b**, Routine testing of head mounted devices for 90 days ( $n=5$  animals). **c**, Normalized weight assessment for 7 postoperative days (POD) after implantation of head mounted device (two-way ANOVA Sidak's multiple comparison test; POD1  $P=0.9998$ , POD2  $P=0.9491$ , POD3  $P>0.9999$ , POD4  $P=0.3731$ , POD5  $P=0.2038$ , POD6  $P=0.9966$ , POD7  $P=0.9966$ ;  $n=5$  naïve &  $n=5$  device animals). **d**, Total distance traveled ( $P=0.6905$ ), **e**, Average speed ( $P=0.5952$ ), **f**, Distance in the outer zone ( $P=0.6905$ ), **g**, Distance in the inner zone ( $P>0.9999$ ), **h**, Time in the outer zone ( $P>0.9999$ ), **i**, Time in the inner zone ( $P=0.5476$ ). (d-i), Locomotion effects of implantation were assessed using the open field test and a variety of parameters were measured (two-tailed unpaired t-test, Mann Whitney test;  $n=5$  naïve &  $n=5$  device animals). **j**, Graphical representation of individual animal behavior, implanted animals (top row) versus naïve controls (bottom row) in the open field test. Outer and inner squares represent the two zones. All data are represented as mean  $\pm$ s.e.m.

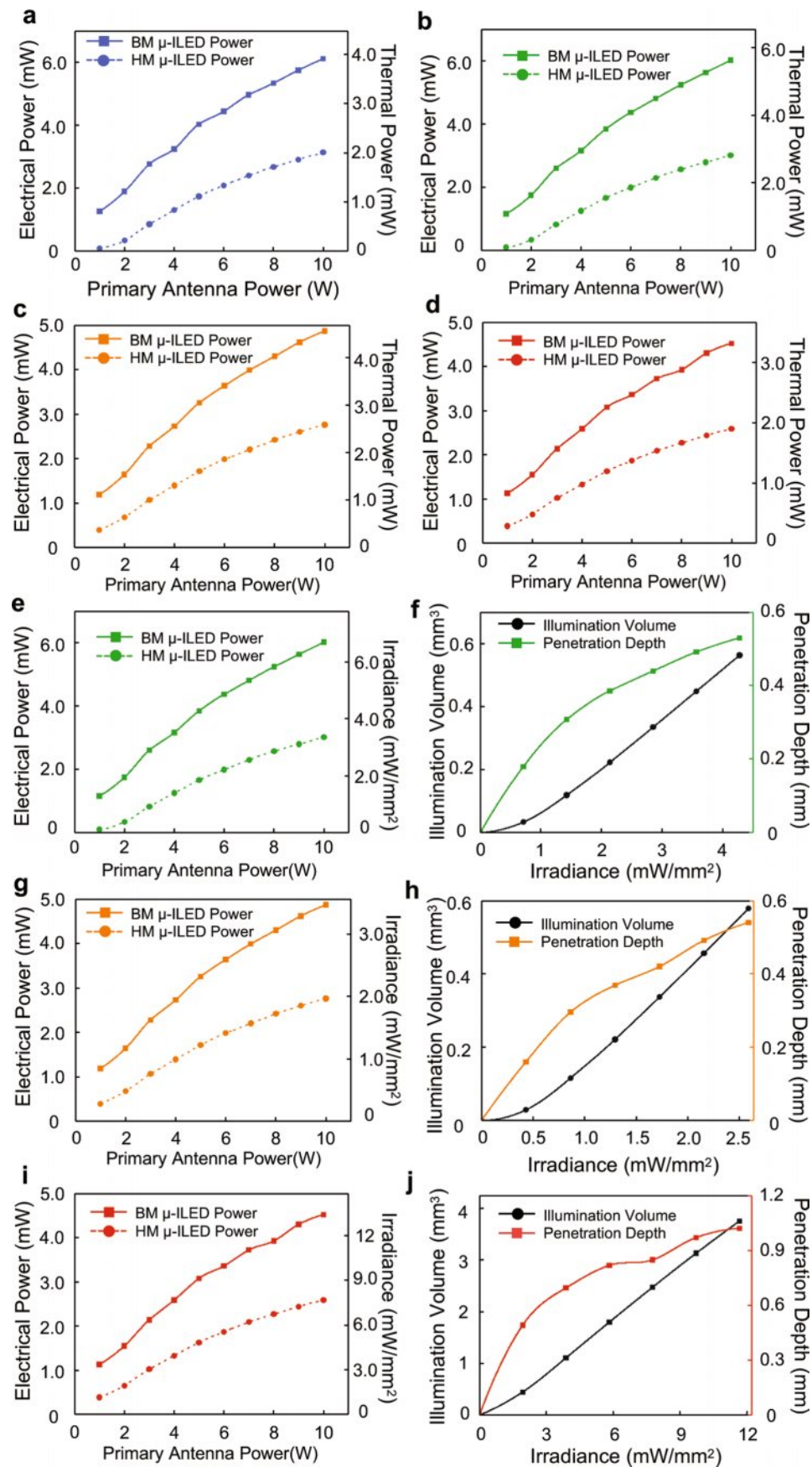


Extended Data Fig. 4 | See next page for caption.

**Extended Data Fig. 4 | Biocompatibility of injectable probes and back mounted implants.** **a**, Astrocytic (GFAP) immunoreactivity surrounding the implantation site of an optical fiber (left) and a wireless probe (right). Scale bar, 200  $\mu\text{m}$ . **b-c**, Same as **(a)**, but for microglia (IBA1) and hemorrhage (hemoglobin subunit  $\alpha$ ). **d**, Summary data showing total astrocyte dense (GFAP) area at different distances from the edge of implantation. Two-way ANOVA, Sidak's multiple comparisons test (Fiber vs Probe), 0-100  $\mu\text{m}$ ,  $P=0.3477$ , 100-200  $\mu\text{m}$ ,  $P=0.4931$ , 200-300  $\mu\text{m}$ ,  $P=0.3285$ , 300-400  $\mu\text{m}$ ,  $p=0.3022$ .  $n=22-23$  slices from 6 brains/group. **e**, Same as **(d)**, but for microglia (IBA1). Two-way ANOVA, Sidak's multiple comparisons test (Fiber vs Probe), 0-200  $\mu\text{m}$ ,  $P=0.7692$ , 200-400  $\mu\text{m}$ ,  $P=0.7414$ .  $n=18$  slices from 6 brains/group. **f**, Same as **(d)**, but for hemorrhage (hemoglobin subunit  $\alpha$ ). Two-tailed unpaired t-test,  $P=0.1054$ .  $n=18$  slices from 6 brains/group. **g**, Summary data show the ratio between measured brain damage and estimated brain damage, based on probe size. Two-tailed unpaired t-test ANOVA,  $P=0.2191$ .  $n=6$  brains/group. **h-i**, H&E staining images show the morphology of the back tissues in mice that went through sham surgery or BM device implantation. Scale bar, 5 mm and 20  $\mu\text{m}$ . **j**, Left, summary data showing average sacrospinalis myofiber size in BM implant and control mice. Two-tailed unpaired t-test,  $P=0.6714$ . Right, cumulative frequency of myofiber size.  $n=10$  slices from 4 animals (Sham),  $n=17$  slices from 6 animals (Device). **k**, Summary data showing the thickness of dermis (left) and subcutaneous tissue (right) in mice after BM implantation of sham surgery. Two-tailed unpaired t-test, Dermis,  $P=0.2650$ , Subcutaneous tissue,  $P=0.9517$ .  $n=16$  slices from 4 animals (Sham),  $n=24$  slices from 6 animals (Device). **l**, Summary data for bone density in mice after sham surgery or BM implantation. Mann Whitney test,  $P=0.0635$ .  $n=4-5$  animals/group. **d-f, j, and k**, white open circles: average value for each animal, grey filled circles: value for individual ROIs/brain slices.

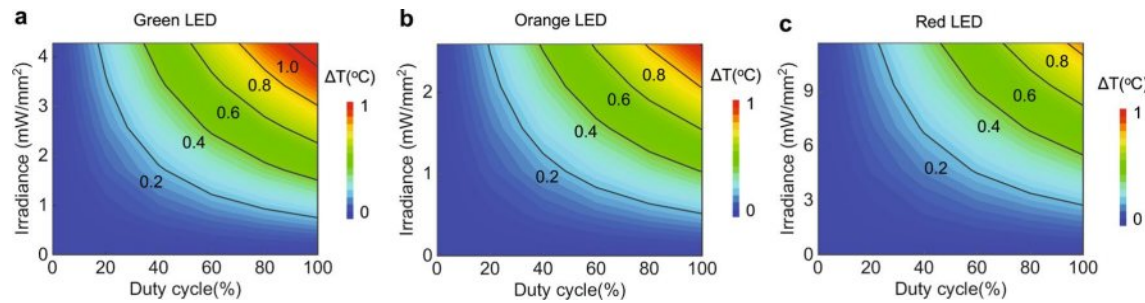


**Extended Data Fig. 5 | Dynamically programmable platform operation with intensity control.** **a**, Generic time diagram that depicts the dynamic parameters accessible via NFC programming. Each channel supports amplitude modulation with signal/carrier defined by period  $T_1/T_2$  and duty cycle  $DC_1/DC_2$ , respectively. **b**, Voltage control implemented by amplitude modulation and its frequency interaction with a passive low-pass filter with cut-off frequency at  $f_c$ . While the information signal contained in its low order harmonics,  $f_{01} < f_c$ , passes almost unchanged, the high frequency carrier,  $f_{02} > f_c$ , is filtered to its direct current component, which is proportional to the duty cycle of the carrier. **c**, Multichannel operation mode representation. This platform allows single channel operation addressed individually, dual operation of any arbitrary channel combination with two modes, in-phase and out-of-phase.

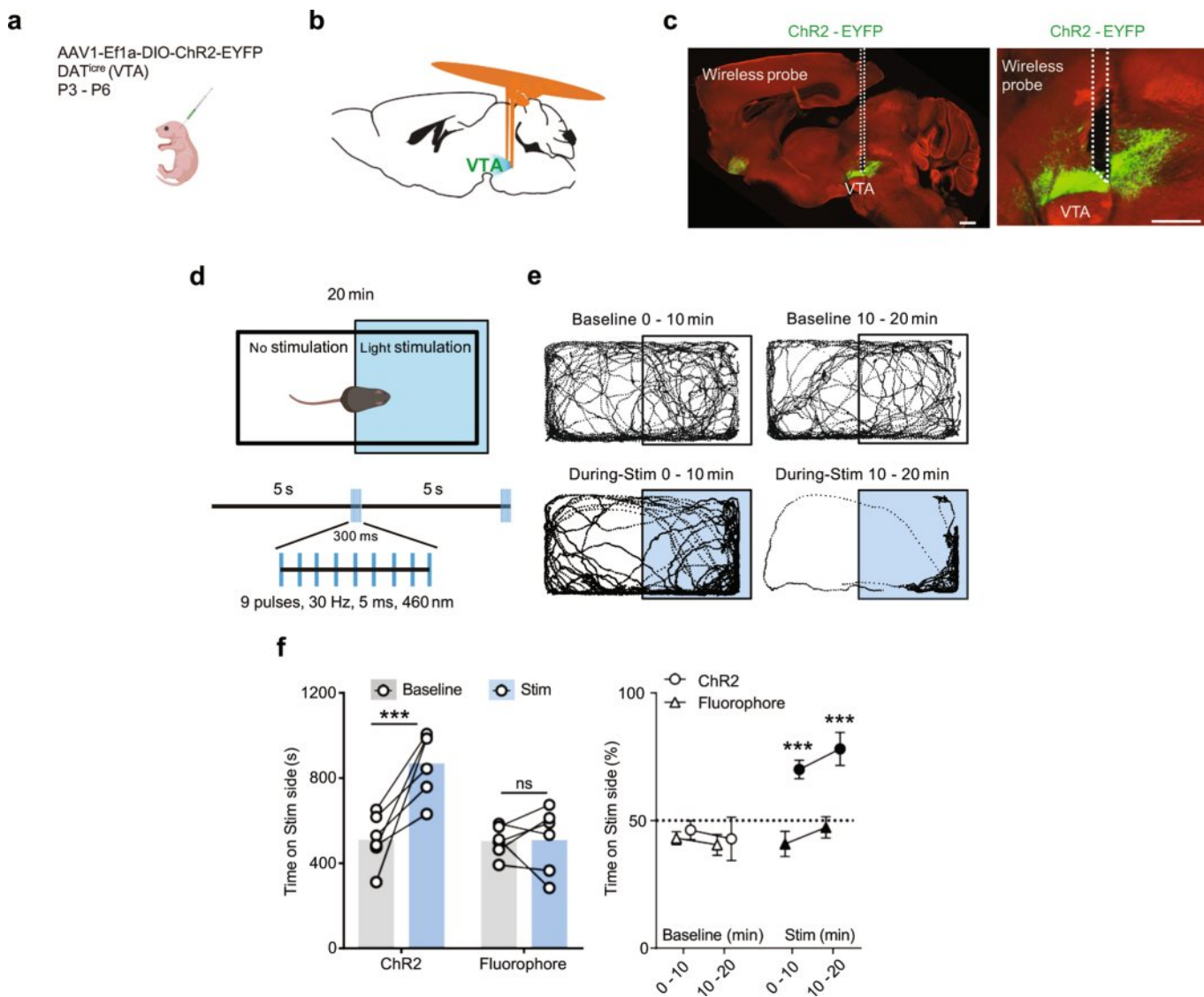


Extended Data Fig. 6 | See next page for caption.

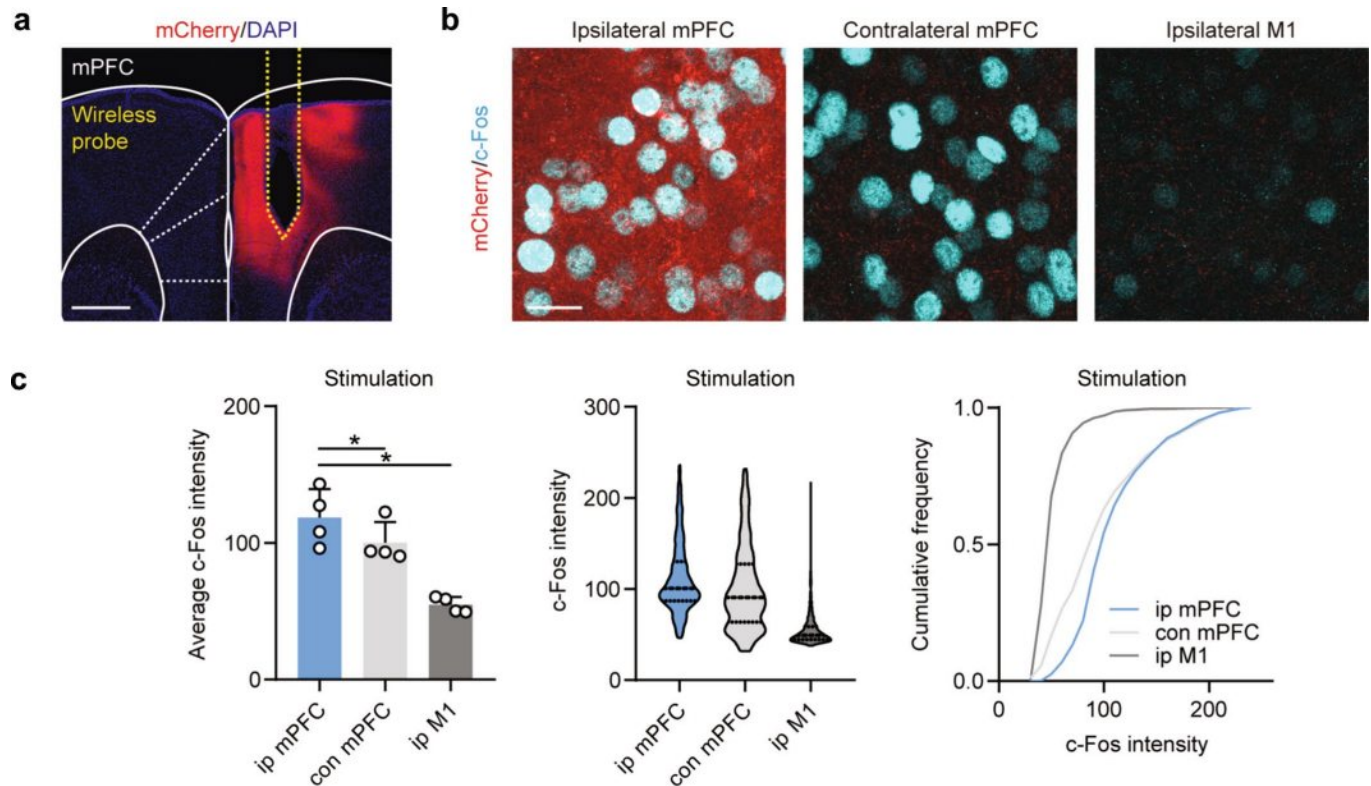
**Extended Data Fig. 6 | Thermal power, irradiance, illumination volume, and penetration depth of  $\mu$ -ILEDs.** **a**, Maximum electrical and thermal power for a single blue  $\mu$ -ILED (460 nm) as a function of RF power applied to the transmission antenna for HM and BM devices. **b, c, d**, Same measurements as reported in **(a)** for green (535 nm), orange (590 nm), and red (630 nm)  $\mu$ -ILEDs respectively. **e**, Maximum electrical and optical irradiance for a single green  $\mu$ -ILED (535 nm) as a function of RF power applied to the transmission antenna for HM and BM devices. **f**, Illumination volume and penetration depth as a function of optical irradiance from a green  $\mu$ -ILED (535 nm; cutoff intensity  $0.1 \text{ mW/mm}^2$ ). **g, h**, Same measurements and simulations as reported in **(e)** and **(f)** respectively for an orange  $\mu$ -ILED (590 nm). **i, j**, Same measurements and simulations as reported in **(e)** and **(f)** respectively for a red  $\mu$ -ILED (630 nm).



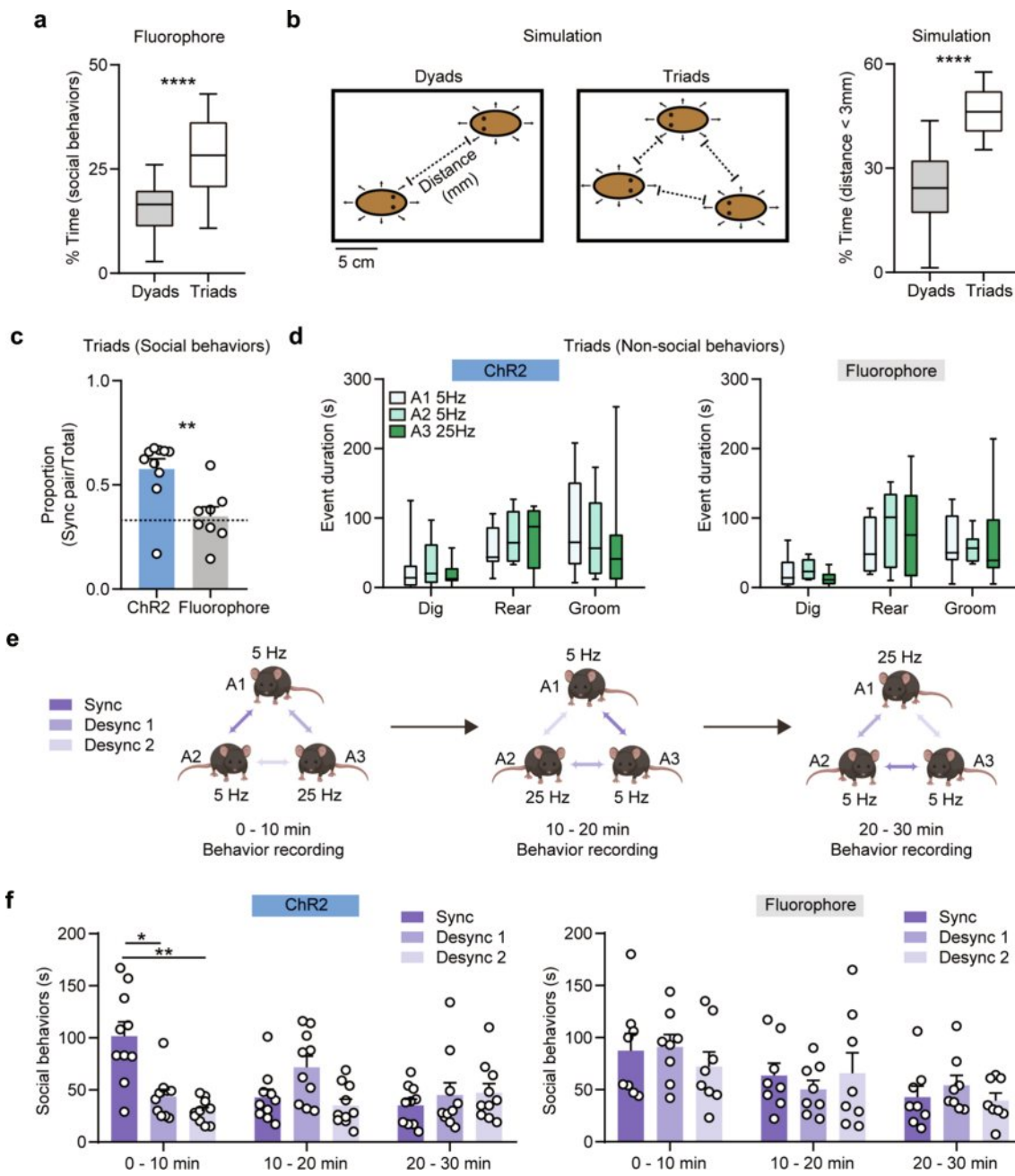
**Extended Data Fig. 7 | Temperature increment vs irradiance and duty cycle at 20 Hz frequency.** **a**, Temperature change at the interface between the encapsulated  $\mu$ -ILED and brain tissue as a function of operational irradiance of green  $\mu$ -ILED (535 nm) and its duty cycle at 20 Hz frequency. **b, c**, Same simulation as reported in **(a)** for orange (590 nm) and red (630 nm)  $\mu$ -LEDs, respectively.



**Extended Data Fig. 8 | Bilateral burst wireless stimulation of midbrain dopaminergic neurons regulates place preference.** **a**, Schematic illustration of neonatal virus transduction in DAT<sup>Cre</sup> animals. **b**, Schematic image of implanted position of bilateral wireless device posterior to the VTA. **c**, Left: sagittal brain section showing the expression of ChR2.EYFP in the VTA and the track of wireless probe. Right: Close up image of the VTA. Scale bar: 500  $\mu$ m. **d**, Top: schematic showing the arena of real-time place preference (RTPP) and the stimulation area (blue). Bottom: burst pattern of wireless optogenetic stimulation. **e**, Example traces showing the tracks of positions in different test periods from one animal. Top: baseline condition without stimulation in the first and last 10 min of the testing session. Bottom: same period of test session, but with light stimulation (460 nm). **f**, Left: summary data showing the total time spent on the antenna side in baseline and stimulation conditions. Two-way ANOVA, Sidak's multiple comparisons test (Baseline vs Stim), ChR2, P = 0.001, Fluorophore, P = 0.9962. Right: percentage of time spent on the antenna side in different testing period. Two-way ANOVA, Sidak's multiple comparisons (Stim, ChR2 vs Fluorophore), 0 - 10 min, P = 0.0008, 10 - 20 min, P = 0.0005. N = 6 mice/group. All data are represented as mean  $\pm$  s.e.m.



**Extended Data Fig. 9 | Increased excitability of mPFC pyramidal neurons after stimulation.** **a**, Image of viral expression of ChR2.mCherry and probe placement. Scale bar, 500  $\mu$ m. **b**, Images of c-Fos immunoreactivity in ipsilateral mPFC, interconnected contralateral mPFC, and ipsilateral M1 as a control region. Scale bar, 20  $\mu$ m. **c**, Summary data show average c-Fos intensity in individual mice (left), the distribution of c-Fos neuronal particle intensities (middle), and cumulative frequency of c-Fos particle intensities. RM one-way ANOVA,  $P=0.0025$ , Sidak's multiple comparisons test, ipsilateral (ip) mPFC vs ipsilateral M1,  $P=0.0201$ , contralateral (con) mPFC vs ipsilateral M1,  $P=0.0370$ .  $N=4$  mice/group. Data represent mean  $\pm$ s.e.m.; dashed lines in the violin plot show quartiles and median. \*  $P < 0.05$ .



**Extended Data Fig. 10 | Wireless control of social behavior in dyads and triads.** **a**, Summary data show the percentage of time spent in social interaction for individual mice in dyads and triads, unpaired two-tailed t-test,  $P < 0.0001$ .  $N = 10$  independent experiments (Dyads),  $N = 8$  independent experiments (Triads). **b**, Left, Schematic illustrating simulation of subject proximity in dyads and triads. Right, estimated percent of time spent in proximity to another subject (distance  $< 3$  mm) for simulated individual in dyads and triads. Unpaired two-tailed t-test,  $P < 0.0001$ .  $N = 30$ /group. **c**, Summary data show the proportion of time spent in social interactions within the synchronized pair, over the total social interaction time for each experiment. Unpaired two-tailed t-test, ChR2 vs Fluorophore,  $P = 0.0044$ .  $N = 10$  independent experiments (ChR2),  $N = 8$  independent experiments (Fluorophore). **d**, Summary data for non-social event durations for ChR2-expressing (left) and fluorophore control (right) mice. Two-way ANOVA, Sidak's multiple comparisons test (main column effect), ChR2: A1 vs A2,  $P = 0.9991$ , A1 vs A3,  $P = 0.8996$ , A2 vs A3,  $P = 0.8420$ . Fluorophore: A1 vs A2,  $P = 0.7711$ , A1 vs A3,  $P = 0.9661$ , A2 vs A3,  $P = 0.9586$ .  $N = 10$  independent experiments (ChR2),  $N = 8$  independent experiments (Fluorophore). **e**, Schematic showing experimental design for 3 mouse social preference and real-time switching of synchronized pairs. **f**, Summary data for the total time spent engaged in social interactions for synchronized or desynchronized pairs across all test sessions. Two-way ANOVA, Sidak's multiple comparisons test, ChR2 0 - 10 min, Sync vs Desync 1,  $P = 0.0198$ , Sync vs Desync 2,  $P = 0.0022$ , other comparisons,  $P > 0.1$ .  $N = 10$  independent experiments (ChR2),  $N = 8$  independent experiments (Fluorophore). Data represent mean  $\pm$  s.e.m. in bar graphs; box and whisker plots show quartiles and median. \*  $P < 0.05$ , \*\* $P < 0.01$ , \*\*\*\* $P < 0.0001$ .

## Supplementary information

# Wireless multilateral devices for optogenetic studies of individual and social behaviors

---

In the format provided by the authors and unedited

## Supplementary Figure 1 – Simple head-mounted devices

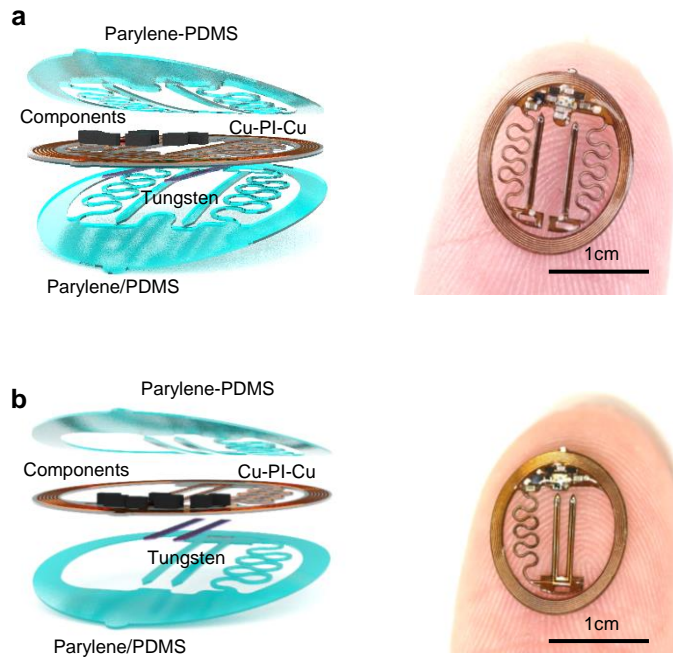


**Figure S1. Simple head-mounted devices.** **a**, Schematic illustrations (left) and photograph (right) of a head mounted device with independent bilateral probes that connect to stretchable serpentines. This device provides voltage regulation. **b**, Schematic illustrations (left) and photograph (right) of a head mounted device with dependent bilateral probes that connect to stretchable serpentines. This device also provides voltage regulation.

**Supplementary Figure 2 – Implantation process for the simplified head-mounted device for mice**

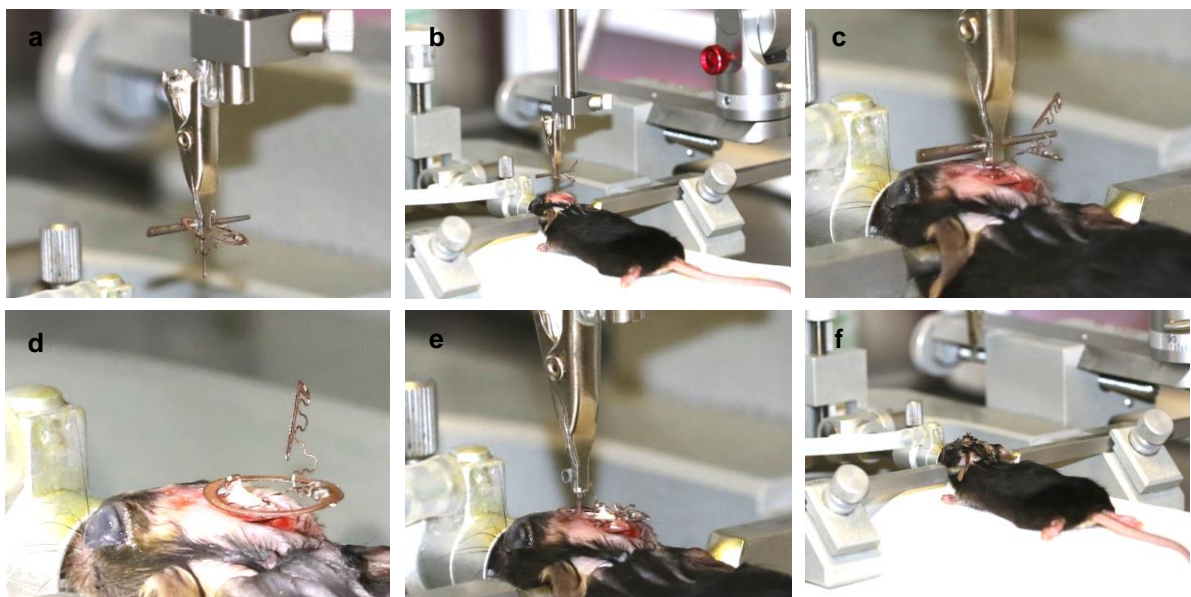


**Figure S2. Implantation process for the simplified head-mounted device for mice.** **a**, Clamp the first probe with a surgical clip that mounts on a stereotaxic apparatus. **b**, Confirm the implantation coordinates. **c**, Drill holes on coordinate locations and inject the first probe into the brain. **d**, Use dental cement to fix the position of the injected probe. **e**, Inject the second probe following the same steps shown in (e)-(d). **f**, Suture the incision on the skin and proceed with post-surgical procedures and monitoring according to institutional guidelines.

**Supplementary Figure 3 – Implantation process for the head-mounted device with dynamically programmable channel operation system for mice**

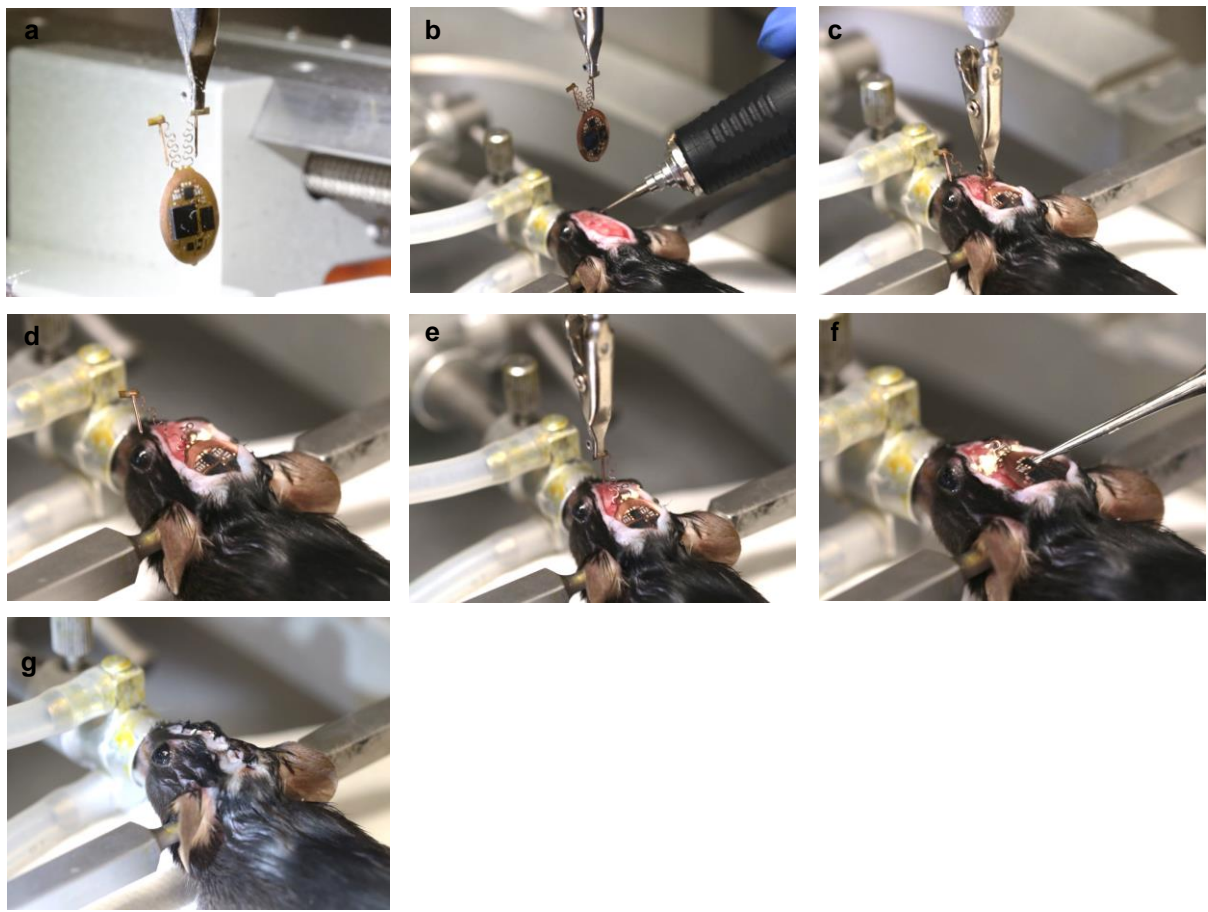


**Figure S3. Implantation process for the head-mounted device with dynamically programmable channel operation system for mice.** **a**, Clamp the first probe with a surgical clip that mounts on a stereotaxic arm. **b**, Confirm the implantation coordinates and drill injection holes in the skull. **c**, Inject the first probe into the brain. **d**, Use cyanoacrylate to fix the position of the injected probe. **e**, Inject the second probe. **f**, Use cyanoacrylate to fix the position of the second injected probe. **g**, Suture the incision on the skin and proceed with post-surgical procedures and monitoring according to institutional guidelines.

## Supplement Figure 4 – Implantation process for the back-mounted device for mice



**Figure S4. Implantation process for the back-mounted device for mice.** **a**, Cut the skin on the head and expose the skull. **b**, Make an incision on the back. **c**, Open a pocket through scalp incision towards back incision. **d**, Confirm the implantation coordinates and drill injection holes in the skull. **e**, Implant the device subdermally through the scalp incision. **f**, Pull the device towards back incision. **g**, Inject the first probe. **h**, Inject the second probe. **i**, Use dental cement to fix positions of injected probes. **j**, Suture the incision on the skin and proceed with post-surgical procedures and monitoring according to institutional guidelines.

**Supplement Figure 5 – Implantation process for the back-mounted device for rats**

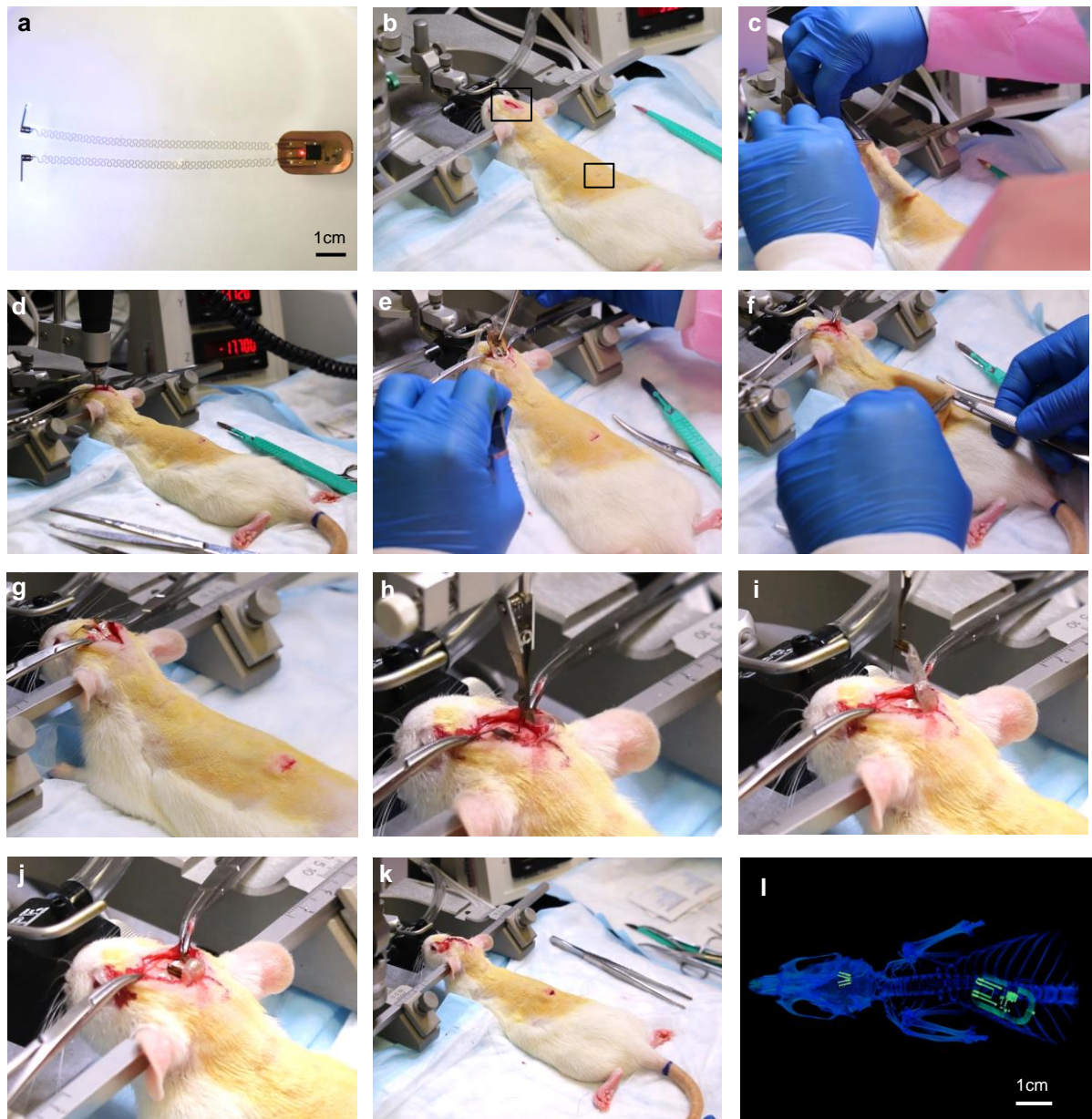


**Figure S5. Implantation process for the back-mounted device for rats.** **a**, Photograph of back subdermally mounted power regulated bilateral device for rats. **b**, Cut incisions on the head and the back. **c**, Open a pocket through head incision towards back incision. **d**, Confirm the implantation coordinates and drill injection holes in the skull. **e**, Implant device subdermally through head incision. **f**, Slide device towards back incision. **g**, Adjust the device position. **h**, Inject the first probe and secure with cyanoacrylate. **i**, Inject the second probe and secure with cyanoacrylate. **j**, Use dental cement to fix positions of injected probes. **k**, Suture the incision on the skin and proceed with post-surgical procedures and monitoring according to institutional guidelines. **l**, CT image of implanted back subdermal device in rat.

**Supplementary Figure 6 – Fabrication scheme for the receiver coil and the electronic system of the back-mounted device**

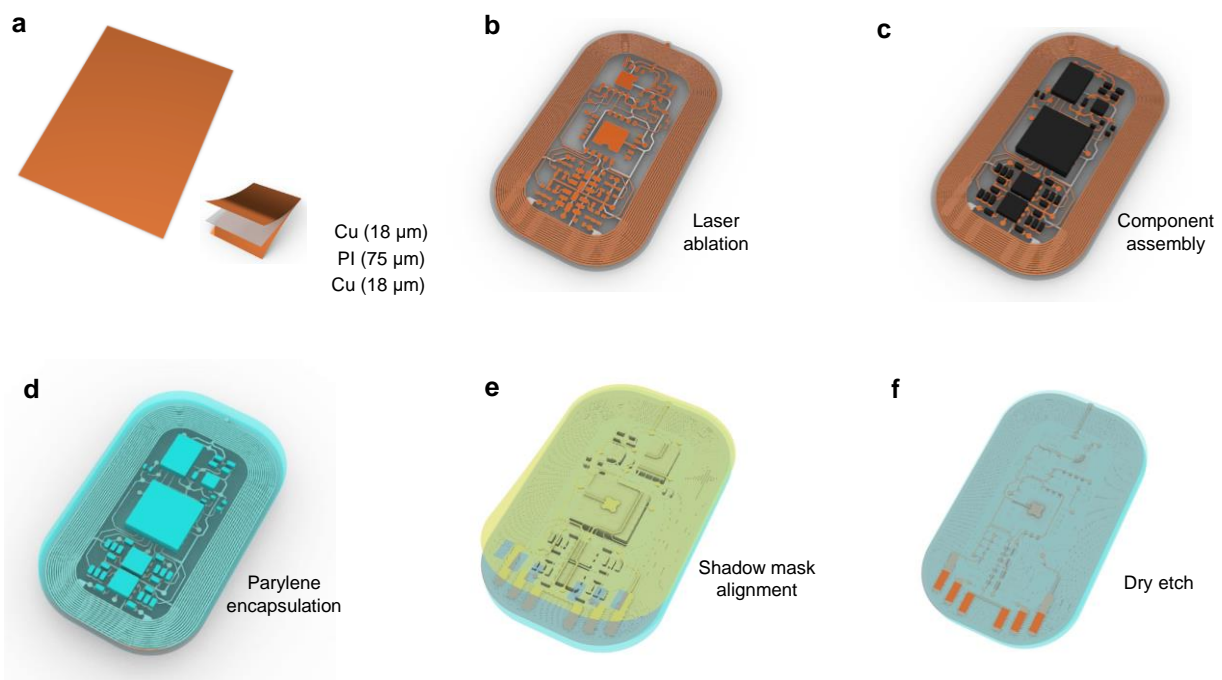


**Figure S6. Fabrication scheme for the receiver coil and the electronic system for the back-mounted device.** **a**, Prepare Pyralux Cu (18 µm)/PI (75 µm)/Cu (18 µm) sheet. **b**, Use laser to cut receiver coil and circuit footprint. **c**, Assemble electronic components. **d**, Coat parylene (14 µm). **e**, Attach PI (75 µm) shadow mask with contact pads exposed. **f**, Etch exposed parylene on contact pads for connection.

## Supplementary Figure 7 – Fabrication scheme for the probes of the back-mounted device

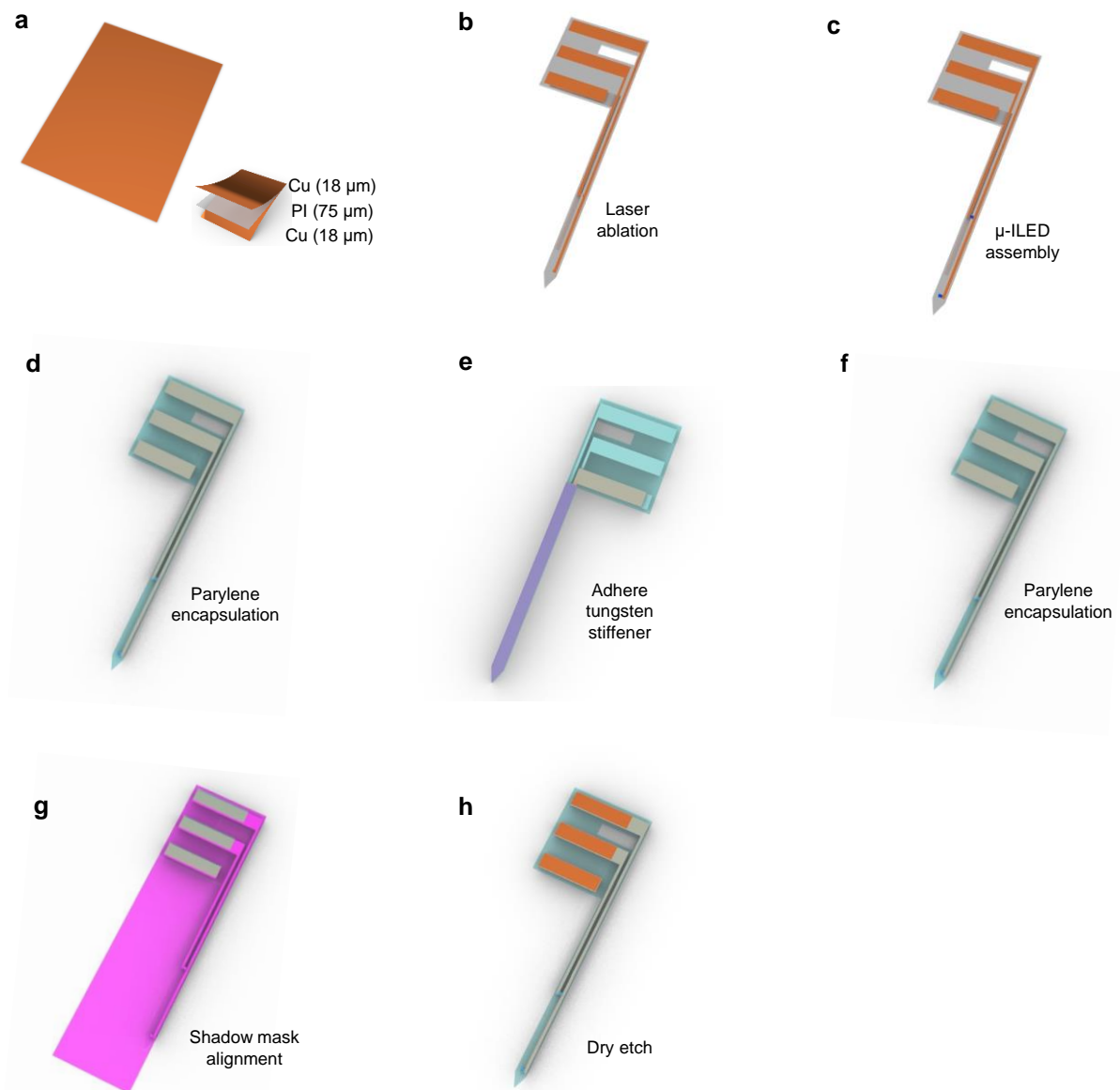


**Figure S7. Fabrication scheme for the probes of the back-mounted device.** **a**, Prepare Pyralux Cu (18 µm)/PI (75 µm)/Cu (18 µm) sheet. **b**, Use laser to cut probe geometry. **c**, Assemble µ-ILEDs. **d**, Coat parylene (14 µm). **e**, Adhere tungsten stiffener with thin layer of epoxy. **f**, Coat parylene (14 µm). **g**, Attach PI (75 µm) shadow mask with contact pads exposed. **h**, Etch exposed parylene on contact pads for connection.

**Supplementary Figure 8 – Fabrication scheme for the soft serpentine traces of the back-mounted device**

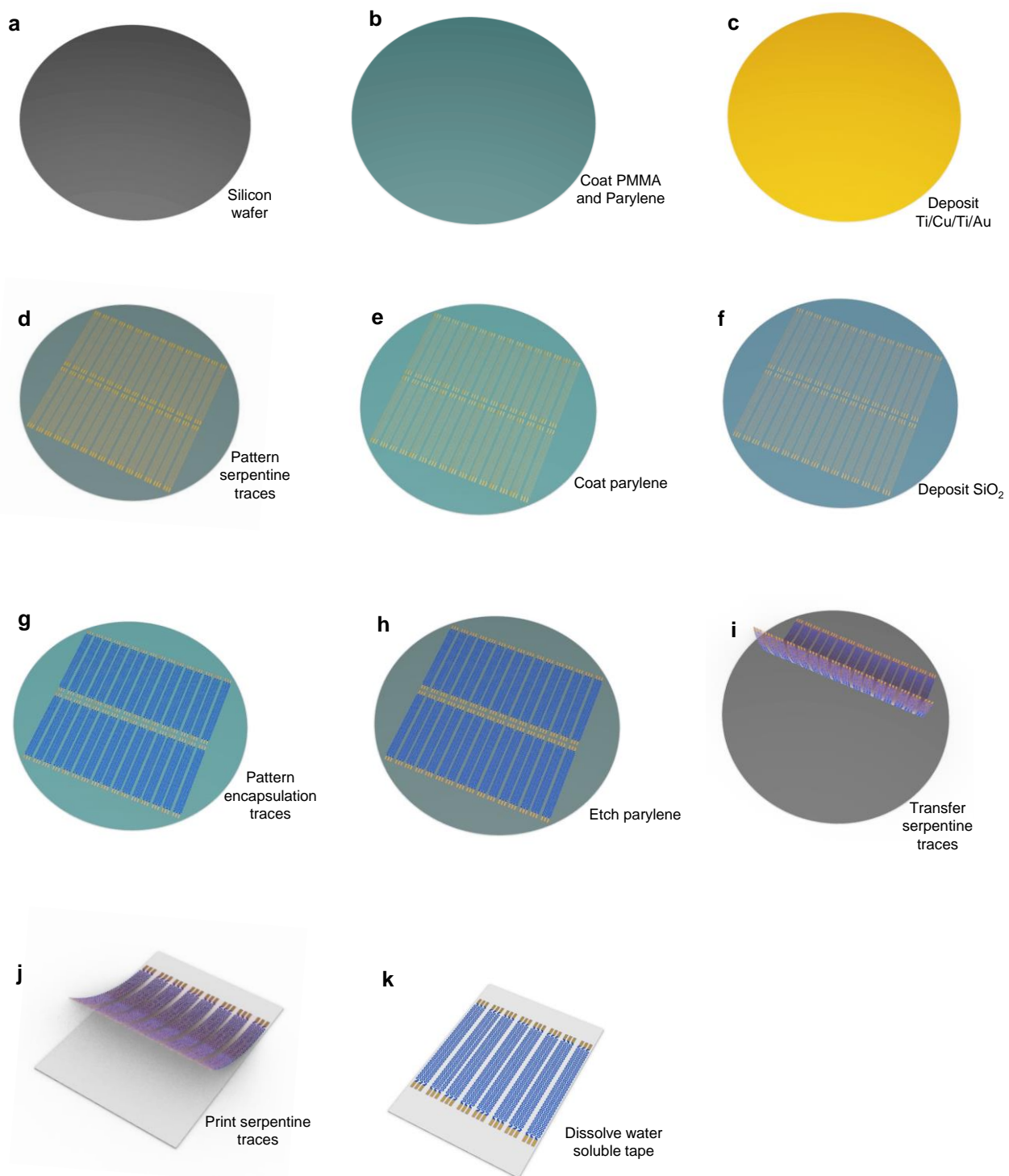


**Figure S8. Fabrication scheme for the soft serpentine traces of the back-mounted device.** **a**, Prepare silicon wafer. **b**, Coat PMMA (500 nm) and parylene (5  $\mu$ m). **c**, Deposit Ti (20 nm)/Cu (300 nm)/Ti (20 nm)/Au (50 nm). **d**, Lithographically pattern metal serpentine traces. **e**, Coat parylene (5  $\mu$ m). **f**, Deposit SiO<sub>2</sub> (60 nm). **g**, Pattern serpentine traces that encapsulate the metal traces with connection pads exposed on SiO<sub>2</sub> through lithography and RIE etching. **h**, Etch parylene through RIE. **i**, Dissolve PMMA and transfer serpentine traces with water soluble tape. **j**, Deposit 30 nm SiO<sub>2</sub> on water soluble tape and print serpentine traces on plasma treated Ecoflex. **k**, Dissolve water soluble tape in DI water.

### Supplementary Figure 9: Pulse voltage modulation

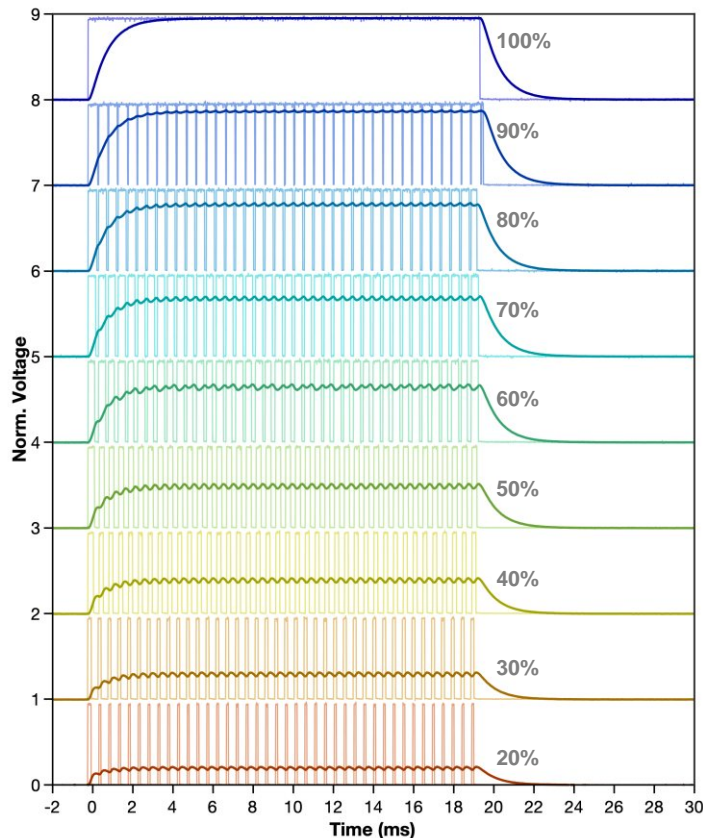


**Figure S9. Pulse voltage modulation.** Signal traces that illustrate the evolution of the signal as it passes the second order passive low-pass filter. The microcontrollers output a low frequency signal (10 Hz in this example at 20% duty cycle) that amplitude modulates a high frequency (2 kHz) carrier. The filtered pulse voltage depends on the duty cycle of the carrier as shown in the figure for duty cycles from 20 to 100%. In the absence of the second order low pass filter this mode of operation provides programmable burst mode of operation.

## Supplementary Figure 10: Demonstration of pulse duration limits

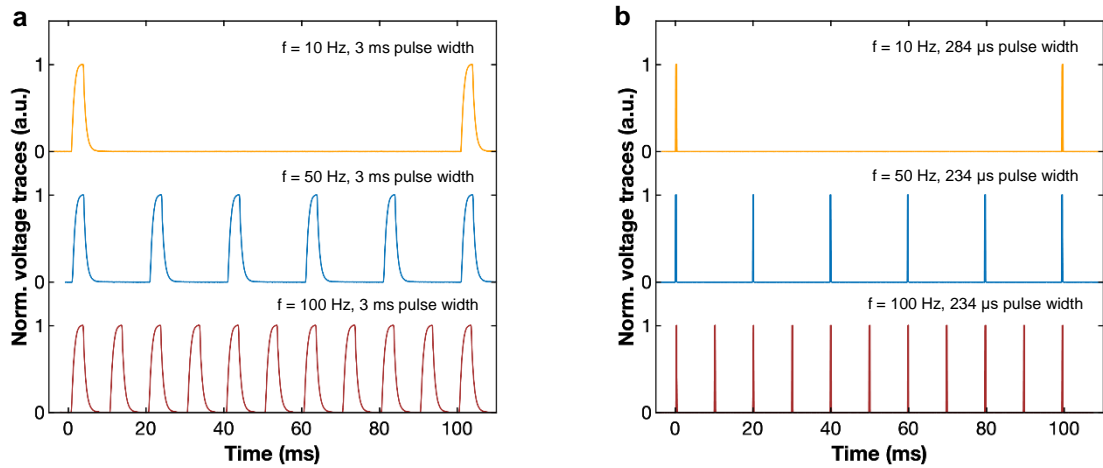


**Figure S10. Demonstration of pulse duration limits.** **a**, The shortest pulse achievable in the system that includes intensity control is 3 ms. The minimum pulse width is limited by the time constant of the analog filter used in the pulse width modulation (PWM) to analog conversion. **b**, In the system without the intensity control module, the achievable pulse widths are as short as 234  $\mu$ s.

**Supplementary Figure 11 – Schematic and operation of the control system**

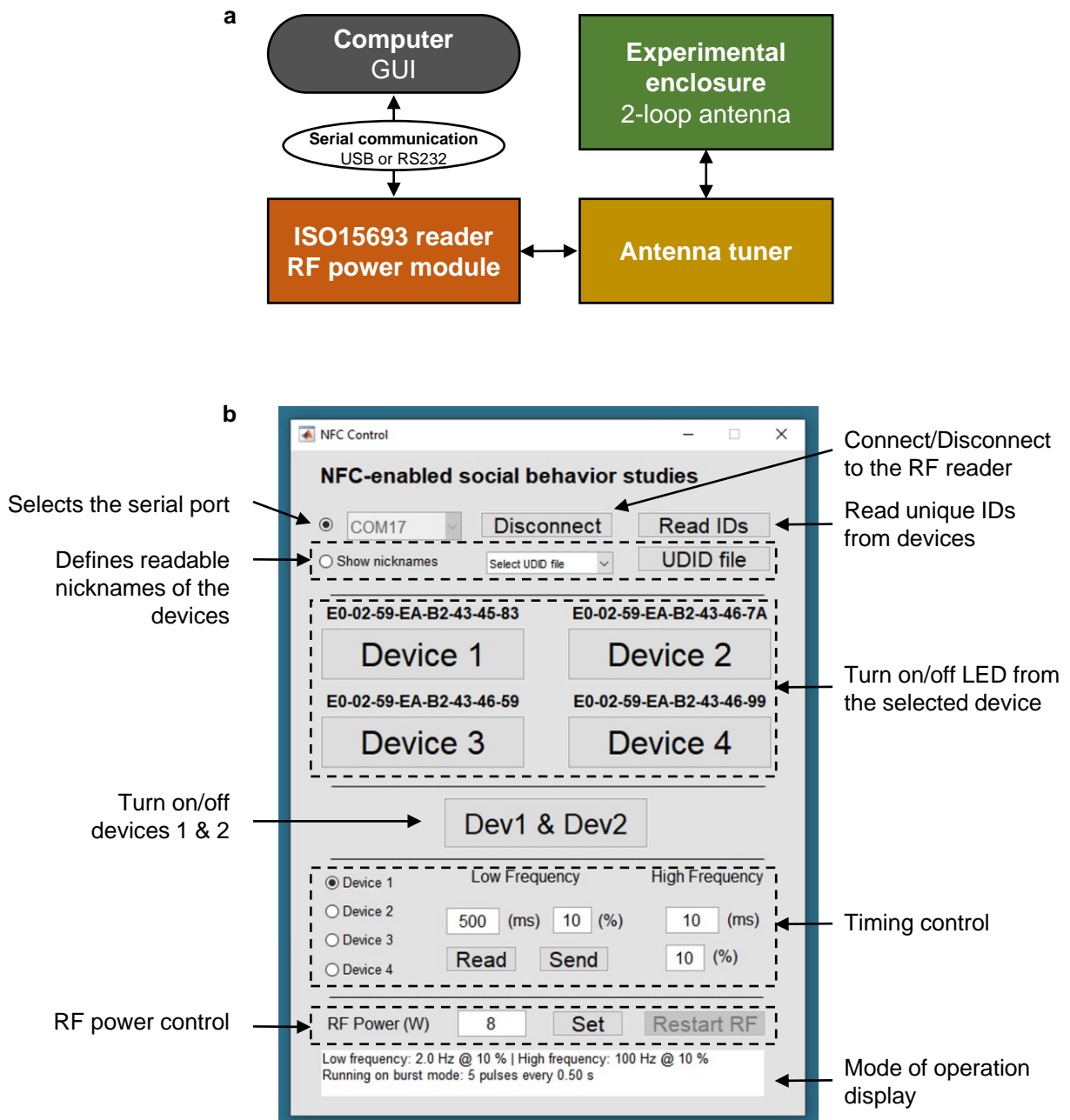


**Figure S11. Schematic and operation of the control system.** **a**, The control system is implemented in a custom-built MATLAB graphical user interface (GUI) that connects to a radio frequency (RF) power module and ISO15693 compliant reader via USB or serial RS232 interface. The GUI implements the corresponding NFC read/write commands addressed to the individual NFC chips contained in each active optogenetic device. The RF power module powers a dual loop antenna wrapped around the experimental enclosure and operating at 13.56 MHz. The antenna tuner provides impedance matching to resonantly transfer RF power and communication signals. Devices contained within the experimental enclosure can be individually addressed and controlled, as the basis for advanced behavioral studies. **b**, Graphical user interface implemented in MATLAB that enables the individual control of up to four devices in the experimental enclosure employed in the three-mice behavior paradigm studied in this work. The GUI also allows the modification of parameters such as the frequency, duty-cycle and RF power levels.

## Supplementary Figure 12: LED characteristics

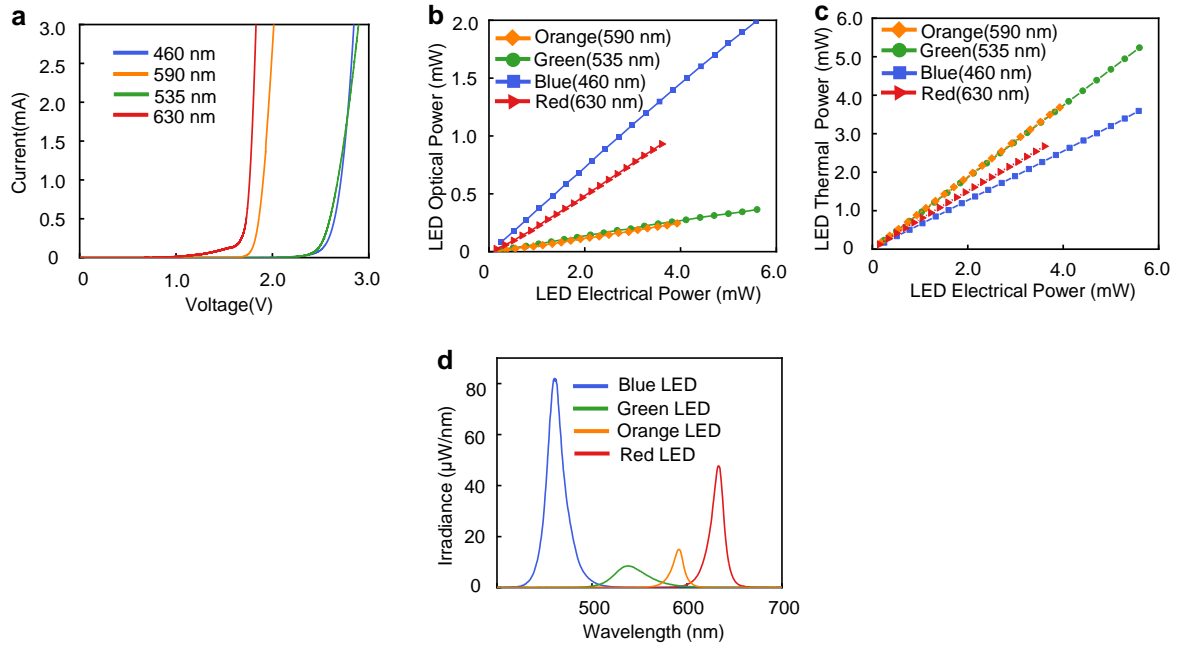


**Figure S12. LED characteristics.** **a**,  $\mu$ -ILED IV curves (460 nm, 535 nm, 590 nm, 630 nm). **b**,  $\mu$ -ILED optical power vs.  $\mu$ -ILED electrical power for different wavelengths (460 nm, 535 nm, 590 nm, 630 nm). **c**,  $\mu$ -ILED thermal dissipation vs.  $\mu$ -ILED electrical power for different wavelengths (460 nm, 535 nm, 590 nm, 630 nm). **d**,  $\mu$ -ILED emission spectra.

## Supplementary Figure 13 – Optical emission profile of $\mu$ -ILED

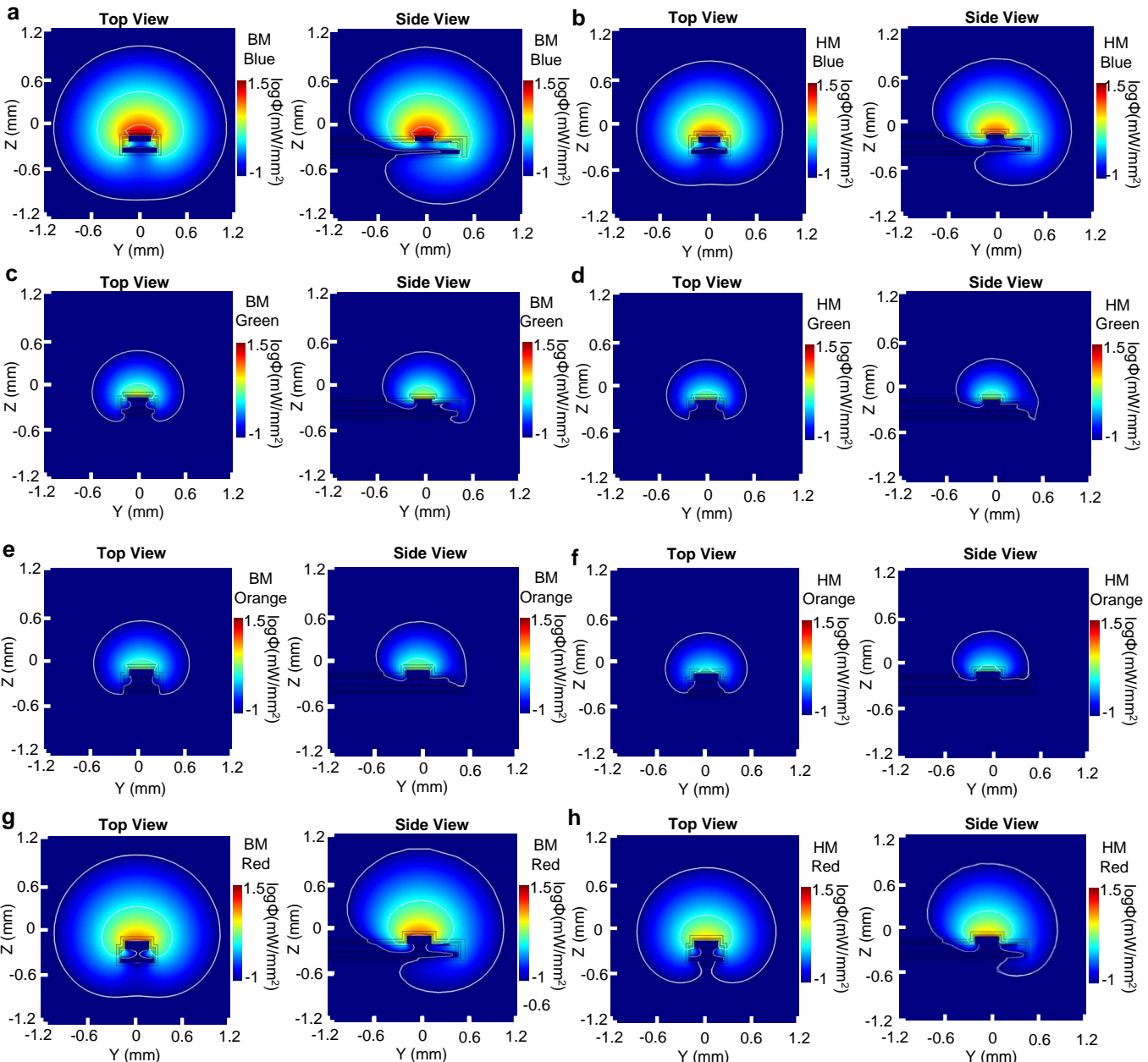


**Figure S13. Optical emission profile of  $\mu$ -ILED.** **a,b**, Simulation of light penetration (460 nm) through brain tissue for back-mounted (BM) and head-mounted (HM) devices wirelessly powered with 8W of RF power applied to a transmission antenna. **c,d**, Simulation of light penetration (535 nm) through brain tissue for BM and HM devices wirelessly powered with 5W (to prevent overheating) and 8W of RF power applied to a transmission antenna. **e,f**, Simulation of light penetration (590 nm) through brain tissue for BM and HM device wirelessly powered with 6W and 8W of RF power applied to a transmission antenna. **g,h**, Simulation of light penetration (630 nm) through brain tissue for BM and HM device wirelessly powered with 8W of RF power applied to a transmission antenna.

**Supplementary Figure 14 – Irradiance penetration profile associated with an  $\mu$ -ILED operating in the brain**

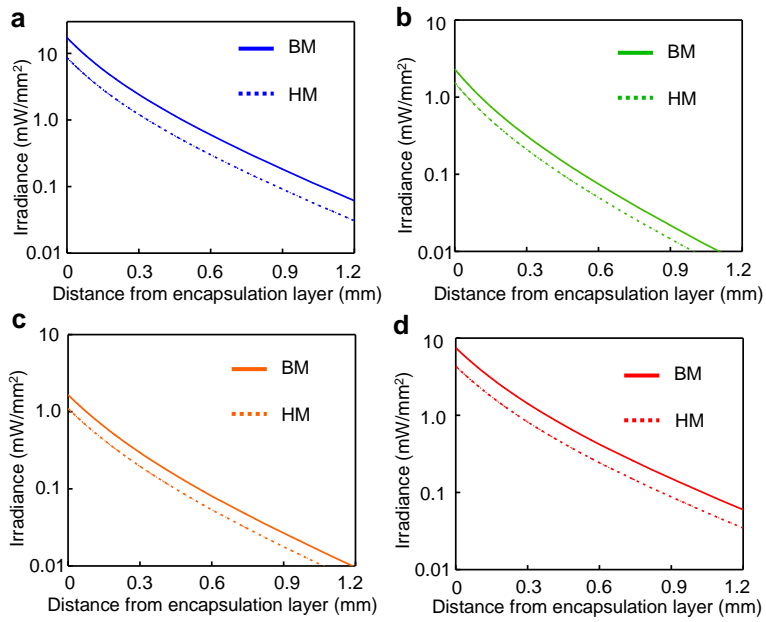


**Figure S14. Irradiance penetration profile associated with an  $\mu$ -ILED operating in the brain.** **a,** Simulated irradiance as a function of penetration depth in brain tissue (460 nm). **b, c, d,** Same simulation as reported in (a) for different wavelengths at 535 nm, 590 nm, and 630 nm respectively.

**Supplementary Figure 15 – Simulation results for changes in probe temperature during operation at 20 Hz and 40% duty cycle, for a BM device with different  $\mu$ -ILEDs**

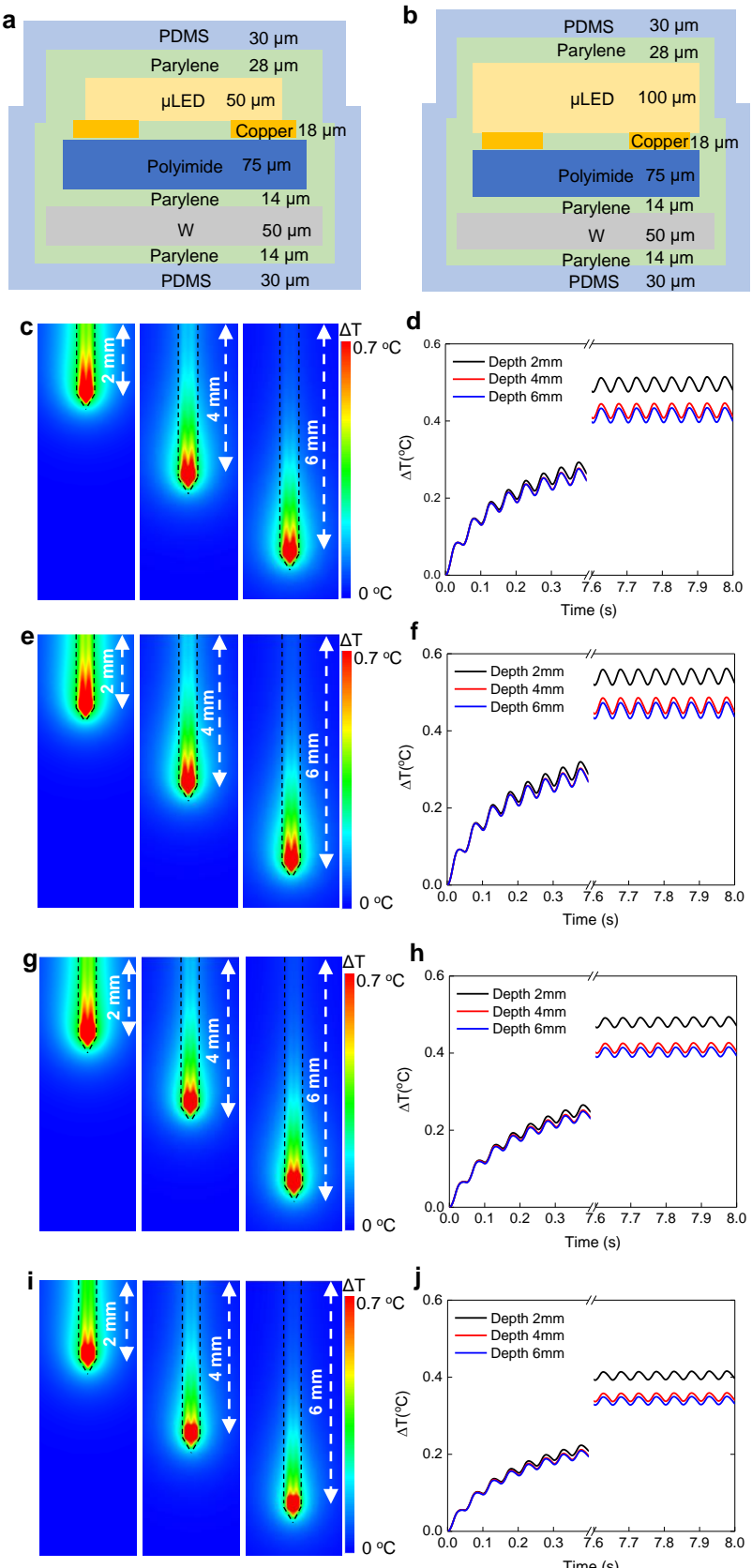


**Figure S15. Simulation results for changes in probe temperature during operation at 20 Hz and 40% duty cycle, for a BM device with different  $\mu$ -ILEDs.** **a**, Cross sectional view of the encapsulation layout for probes with a blue (460 nm) or a green (535 nm)  $\mu$ -ILED. **b**, Cross sectional view of the encapsulation layout for probes with an orange (590 nm) or a red (630 nm)  $\mu$ -ILED. **c**, Simulated distribution of the change in temperature across the probe/tissue interfaces during operation (460 nm) at implantation depths of 2 mm, 4 mm, and 6 mm. **d**, Simulated distribution of the change in temperature at the probe tip (highest temperature) during operation (460 nm) as a function of time at implantation depths of 2 mm, 4 mm, and 6 mm. **e, f**, Same simulation as reported in (c) and (d) respectively for green (535 nm)  $\mu$ -ILED. **g, h**, Same simulation as reported in (c) and (d) respectively for orange (590 nm)  $\mu$ -ILED. **i, j**, Same simulation as reported in (c) and (d) respectively for red (630 nm)  $\mu$ -ILED.

**Supplementary Table S1 – Optical & thermal power output for HM and BM devices**

a. Blue  $\mu$ -ILED (460 nm)

	Transmission Antenna Power (W)	Optical Power (mW)	Thermal Power (mW)
HM	8	0.965	1.71
BM	8	1.93	3.41

b. Green  $\mu$ -ILED (535 nm)

	Transmission Antenna Power (W)	Optical Power (mW)	Thermal Power (mW)
HM	8	0.170	2.40
BM	5	0.254	3.60

c. Orange  $\mu$ -ILED (590 nm)

	Transmission Antenna Power (W)	Optical Power (mW)	Thermal Power (mW)
HM	8	0.155	2.27
BM	6	0.233	3.41

d. Red  $\mu$ -ILED (630 nm)

	Transmission Antenna Power (W)	Optical Power (mW)	Thermal Power (mW)
HM	8	0.606	1.66
BM	8	1.05	2.88

**a**, Blue  $\mu$ -ILED (460 nm). **b**, Green  $\mu$ -ILED (535 nm), transmission antenna power at 5 W for BM scenario to prevent overheating. **c**, Orange  $\mu$ -ILED (590 nm), transmission antenna power at 6 W for BM scenario to prevent overheating. **d**, Red  $\mu$ -ILED (630 nm).

**Supplementary Table S2 – Materials/tissue absorption coefficients  $\mu_a$  ( $\text{cm}^{-1}$ ) used in the optical and thermal simulations for different light wavelengths.**

	Blue light (460 nm)	Green light (535 nm)	Orange light (590 nm)	Ref light (630 nm)
Fresh Brain <sup>1</sup>	4.47	5.90	4.90	4.30
Copper <sup>2</sup>	$6.65 \times 10^5$	$6.09 \times 10^5$	$6.00 \times 10^5$	$6.72 \times 10^5$
Tungsten <sup>3</sup>	$5.47 \times 10^5$	$5.47 \times 10^5$	$5.47 \times 10^5$	$5.47 \times 10^5$
Polyimide (PI) <sup>4</sup>	0.879	0.879	0.879	0.879
PDMS <sup>5</sup>	0.153	0.153	0.153	0.153
Parylene <sup>6</sup>	1.62	1.62	1.62	1.62
$\mu$ -ILED <sup>7</sup>	$1.88 \times 10^5$	$7.73 \times 10^4$	$5.12 \times 10^4$	$4.01 \times 10^4$

**Supplementary Table S3 – Materials/tissue reduced scattering coefficients  $\mu'_s$  ( $\text{cm}^{-1}$ ) used in the optical simulations for different light wavelengths**

	Blue light (460 nm)	Green light (535 nm)	Orange light (590 nm)	Ref light (630 nm)
Fresh Brain <sup>1</sup>	50.5	40.8	36.1	31.6
Copper	0	0	0	0
Tungsten	0	0	0	0
Polyimide (PI)	0.01	0.01	0.01	0.01
PDMS	0.001	0.001	0.001	0.001
Parylene	0.001	0.001	0.001	0.001
$\mu$ -ILED	0	0	0	0

**Supplementary Table S4 – Materials/tissue thermal properties used in the heat-transfer simulation**

	Thermal Conductivity $k$ (W·m <sup>-1</sup> ·K <sup>-1</sup> )	Specific Heat Capacity $C_p$ (J·kg <sup>-1</sup> ·K <sup>-1</sup> )	Density $\rho$ (kg·m <sup>-3</sup> )
Fresh Brain	0.5	3700	1050
Copper	377	385	8960
Tungsten	163	134	1930
Polyimide (PI)	0.21	2100	909
PDMS	0.15	1460	970
Parylene	0.084	712	1289
$\mu$ -ILED	130	490	6100

**Supplementary Table S5 – Summary of the bio-heat parameters <sup>8</sup> used in the thermal simulation**

Variable	Parameter	Value	Units
$\rho_b$	Density of Blood	1060	kg·m <sup>-3</sup>
$C_b$	Specific Heat of Blood	3639	J·kg <sup>-1</sup> ·K <sup>-1</sup>
$\omega_b$	Blood Perfusion Rate	0.0085	s <sup>-1</sup>
$Q_{met}$	Metabolic Heat Production (Brain)	9700	W·m <sup>-3</sup>
$T_b$	Arterial (core body) Temperature	309.85	K
$T_o$	Initial Brain Temperature	310.15	K

## References

1. Mesradi, M. *et al.* Experimental and analytical comparative study of optical coefficient of fresh and frozen rat tissues. *J. Biomed. Opt.* **18**, 117010 (2013).
2. Johnson, P. B. & Christy, R. W. Optical Constants of the Noble Metals. *Phys. Rev. B* **6**, 4370–4379 (1972).
3. Ordal, M. A., Bell, R. J., Alexander, R. W., Newquist, L. A. & Querry, M. R. Optical properties of Al, Fe, Ti, Ta, W, and Mo at submillimeter wavelengths. *Appl. Opt.* **27**, 1203 (1988).
4. Zhang, Z. M., Lefever-Button, G. & Powell, F. R. Infrared Refractive Index and Extinction Coefficient of Polyimide Films. *Int. J. Thermophys.* **19**, 905–916 (1998).
5. Querry, M. Optical Constants of Minerals and Other Materials from the Millimeter to the Ultraviolet. 333 (1987).
6. Gatesman, A. J., Waldman, J., Ji, M., Musante, C. & Yngvesson, S. An Anti-Reflection Coating for Silicon Optics at Terahertz Frequencies. *IEEE Microw. Guid. Wave Lett.* **10**, 264–266 (2000).
7. Aspnes, D. E., Kelso, S. M., Logan, R. A. & Bhat, R. Optical properties of  $\text{Al}_x\text{Ga}_{1-x}$ . *As. J. Appl. Phys.* **60**, 754–767 (1986).
8. Stujsenske, J. M., Spellman, T. & Gordon, J. A. Modeling the Spatiotemporal Dynamics of Light and Heat Propagation for In Vivo Optogenetics. *Cell Rep.* **12**, 525–534 (2015).